J. Fluid Mech. (2021), *vol*. 916, A8, doi:10.1017/jfm.2021.159

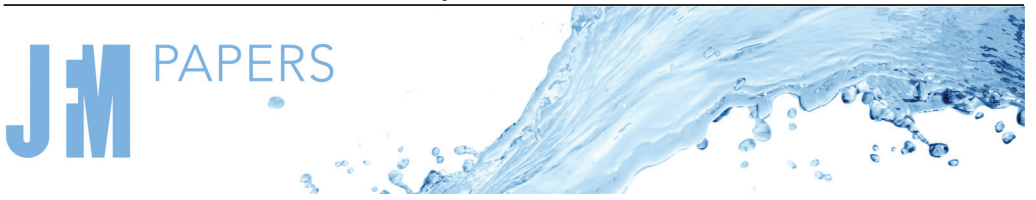

Equatorial modons in dry and moist-convective shallow-water systems on a rotating sphere

Bowen Zhao[1],†, Vladimir Zeitlin[2] and Alexey V. Fedorov[1,3]

[1]Department of Earth and Planetary Sciences, Yale University, 210 Whitney Avenue, New Haven, CT, USA

[2]Laboratory of Dynamical Meteorology, Sorbonne University (SU), Ecole Normale Supérieure (ENS), CNRS, Paris 75231, France

[3]LOCEAN/IPSL, Sorbonne University, 4 place Jussieu, Paris 75252, France

(Received 23 October 2020; revised 6 February 2021; accepted 14 February 2021)

The adjustment of equatorial pressure anomalies is studied using high-resolution numerical simulations within one- and two-layer shallow-water systems on a rotating sphere, which include a simple self-consistent parameterization of the dynamical effects of condensation (the so-called moist-convective shallow-water equations). A systematic generation of localized, moving eastward along the equator cyclonic pairs, termed the equatorial modons, is observed in the one-layer model for sufficiently intense initial perturbations. The modons are strongly enhanced by the moist convection. In the two-layer model with a relatively small depth ratio, baroclinic equatorial modons are also observed. In both the one-layer model and the baroclinic mode of the two-layer model, the emergence of a transient Gill pattern preceding the generation of modons is demonstrated. It is found that the breaking of circumnavigating moist Kelvin waves, generated in the adjustment process, induces extensive easterly jets, which weaken the eastward nonlinear advection tendency of the modons. Finally, an inductive generation of the modons over oceanic warm-pools, modelled as local humidity maxima, is discovered, and explained on the basis of conservation of moist potential vorticity.

Key words: moist convection, atmospheric flows, vortex dynamics

1. Introduction

Rotating shallow-water (RSW) models provide a valuable tool for conceptual understanding of the main features of atmosphere and ocean dynamics at large horizontal scales (e.g. Zeitlin 2018). This is particularly true for the dynamics of the tropical atmosphere, for which the theoretical foundations were laid in the classical studies

† Email address for correspondence: bowen.zhao@yale.edu

by Matsuno (1966) and Gill (1980) who used the simplest one-layer version of the shallow-water model on the equatorial beta-plane. The linearized version of the model, used in their papers, captures a rich spectrum of equatorial waves which play a crucial role in the equatorial atmosphere and ocean and allow computing of the response of the two media to a localized forcing. In the full nonlinear version of the model, specific dispersion properties of long equatorial waves suggest that weakly nonlinear Rossby waves can form westward-propagating solitons (Boyd 1985), while Kelvin waves tend to form Kelvin fronts (e.g. Fedorov & Melville 2000; Bouchut, Le Sommer & Zeitlin 2005). Yet, fully nonlinear Rossby-wave structures, the eastward-propagating modons, were identified in this model only recently (Rostami & Zeitlin 2019*a*). (Notice that KdV-like Rossby-wave solitons were also called 'modons' by Boyd 1985).

The modon solutions of the geophysical fluid dynamics equations were first found in a barotropic quasi-geostrophic (QG) model with a finite deformation radius on a midlatitude tangent plane (the f-plane) in the pioneering paper by Larichev & Reznik (1976), and then were generalized to a two-layer QG model by Flierl *et al.* (1980), to include the effects of baroclinicity. The QG approximation, as such, is not fully valid on the equatorial beta-plane, which, probably, explains why equatorial modon solutions were previously overlooked. Nevertheless, the weak pressure gradient approximation, which was advanced for the tropical atmosphere in the seminal work by Charney (1963), leads to the Charney equation which is identical to the barotropic QG equation with infinite deformation radius, and has the same solutions. (Evidence of non-divergenceless of large-scale tropical motions can be found in the data (Yano & Bonazzola 2009; Yano, Mulet & Bonazzola 2009).) We should recall that the barotropic QG equation with a finite deformation radius, which is also called the Charney–Obukhov equation, is an asymptotic limit of the one-layer RSW model on a midlatitude f-plane at small Rossby numbers, and small nonlinearities. Likewise, the two-layer QG model is an asymptotic limit of the two-layer RSW. Similarly, the Charney equation is an asymptotic limit of the RSW model on the equatorial beta-plane at small pressure variations. Hence, the modon solutions in both cases are asymptotic, at most, and their validity and existence in the full RSW model(s) remained to be proved. This was done, for the modons on a midlatitude f-plane, by Kizner *et al.* (2008) using a semianalytic approach, and later in Ribstein, Gula & Zeitlin (2010) who showed, by direct numerical simulations initialized with asymptotic modon solutions, that these modons underwent an 'ageostrophic adjustment' process and became long-living dipolar coherent structures close to asymptotic modons. The same method applied to two-layer barotropic and baroclinic modons on a midlatitude f-plane (Lahaye & Zeitlin 2012) revealed the transformation of the two-layer QG modons into modon-like solutions of the parent two-layer RSW equations, although of a larger variety depending on the values of key parameters. By the same method it was demonstrated in Rostami & Zeitlin (2019*a*), that asymptotic modons in one-layer RSW on the equatorial beta-plane give rise to more compact eastward-moving equatorial modons.

Previous analytical and numerical studies of the relaxation of localized pressure anomalies in the equator belt (equatorial adjustment) (LeSommer, Reznik & Zeitlin 2004; Rostami & Zeitlin 2019*b*) showed that while the adjustment of weakly nonlinear anomalies with large zonal-to-meridional aspect ratios produces a Kelvin wave to the east, and a Rossby-wave packet to the west of the perturbation, the canonical picture in the long-wave approximation (Gill 1980; Fedorov & Brown 2009), sufficiently deep pressure anomalies with close to one aspect ratio can produce the modon solutions, especially if the effects of moist convection are taken into account. Yet a similar analysis of the two-layer equatorial RSW shows that quasi-barotropic or barolinic modons are less robust than their counterparts on a midlatitude f-plane, and can rapidly disperse (Rostami & Zeitlin 2020*b*).

All of the above-mentioned studies were accomplished using the tangent plane approximation to a rotating sphere. A natural question, which arose soon after the discovery of the modons and is important in the context of large-scale atmospheric motions, is about the transposition of these solutions to a whole sphere. The first answer to this question was given in Tribbia (1984), Verkley (1984) where modon solutions of a barotropic model on a sphere were constructed. However, it is only recently, by using a similar strategy as applied by Ribstein *et al.* (2010) on the tangent plane (the difference being an extremely careful preparation of balanced initial conditions, following Baer & Tribbia 1977), that Yano & Tribbia (2017) showed that the barotropic modon solutions of Tribbia (1984) and Verkley (1984) survived for a long time in the parent one-layer RSW model on a sphere. No results for two-layer modons on a rotating sphere are known in the literature, to the best of our knowledge.

One of the motivations for studying modons is related to the claim of Yano & Tribbia (2017) on the possible relevance of spherical modons to dynamical mechanisms behind the phenomenon of the Madden–Julian Oscillation (MJO). The MJO arises as a planetary-scale eastward-propagating quasi-periodic coherent structure in the tropical Indo-Pacific (e.g. Zhang 2005). The MJO propagation speed is far below the phase speeds of atmospheric eastward-propagating Kelvin and inertia-gravity waves, as seen for example from the dispersion diagram of the equatorial waves inferred from outgoing long-wave radiation (OLR) measurements (Wheeler & Kiladis 1999).

A comprehensive dynamical explanation of the MJO remains one of the challenges in tropical meteorology and climatology. Two recent reviews (Zhang *et al.* 2020; Jiang *et al.* 2020) give a comprehensive picture of the present state of the theory of the MJO and we briefly summarize some below. Already upon its first identification, Madden & Julian (1971) hypothesized that deep convection is crucial for the MJO dynamics. Various theoretical models have been proposed since then for the MJO, in particular those based on the so-called moisture mode, which consider the column-integrated precipitable water as the key variable for the MJO, while a positive feedback between precipitation and moist static energy sources acts as a destabilization mechanism (e.g. Neelin & Yu 1994; Fuchs & Raymond 2002, 2005; Majda & Stechmann 2009; Raymond & Fuchs 2009; Fuchs & Raymond 2017; Khairoutdinov & Emanuel 2018). So-called multiscale models interpret the MJO as a result of atmospheric turbulence where mesoscale waves and convection provide the eddy fluxes that transport energy upscale. Some recent studies interpret the MJO as a convective self-aggregation instability of the radiative-convective equilibrium state on the equatorial beta-plane (Arnold & Randall 2015). There are also studies that consider the MJO as a result of eastward and westward inertia–gravity wave interference (Yang & Ingersoll 2013, 2014), or a wave packet of mixed Rossby-gravity waves (Yang & Ingersoll 2011). The common feature of all these studies is that they usually neglect hydrodynamic nonlinearities, considering moist processes as the only nonlinearity which is relevant, and coupling them to linear atmospheric waves. In particular, nonlinear advection is neglected.

In contrast, the idea of Yano & Tribbia (2017), following the hypothesis of Wedi & Smolarkiewicz (2010) that the MJO could be a nonlinear wave, is that hydrodynamic nonlinearity is crucial, and that the MJO events are, in essence, nonlinear modons. An obvious advantage of the modon theory is that eastward propagation is inherent, as well as small phase speeds, similar to the observed MJO. It should be stressed, however, that convective phenomena were neglected altogether in Yano & Tribbia (2017). Yet, moist convection is an essential ingredient of the dynamics of the tropical atmosphere in general and of the MJO in particular. Dynamical influence of the moist convection

can be included in shallow-water models in a robust and self-consistent way, without sacrificing their simplicity. The corresponding one- and two-layer moist-convective rotating shallow-water (mcRSW) models were derived using vertical averaging of the primitive equations, Lagrangian conservation of equivalent potential temperature, and relaxational parametrisation of condensation in, respectively, Bouchut *et al.* (2009) and Lambaerts *et al.* (2011). They can be used for obtaining conceptual understanding of large-scale dynamical processes in the equatorial region, thus continuing a long tradition of shallow-water modelling of the tropical atmosphere (Matsuno 1966; Gill 1980, 1982; Heckley & Gill 1984; Lindzen & Nigam 1987; Seager 1991) while adding hydrodynamic nonlinearity which was neglected in these papers. Along these lines, Rostami & Zeitlin (2019*b*) revisited the equatorial adjustment problem with the one-layer mcRSW model on the equatorial beta-plane, and demonstrated both the existence of modon solutions and the role of convective processes in their generation and maintenance. Unlike Yano & Tribbia (2017), Rostami & Zeitlin (2019*a*) showed, albeit on a tangent plane, that due to the effects of moisture modons arise from 'unprepared', unbalanced and rather arbitrary initial perturbations, which reinforces the idea of their relevance to equatorial dynamics.

In the present paper, motivated by the recent studies, we investigate the generation of equatorial modons by the process of equatorial adjustment, and their interactions with equatorial waves, on a whole sphere, without limitations of the equatorial beta-plane, and in both dry and moist-convective environments. We perform direct numerical simulations with one- and two-layer mcRSW models using a code based on recent advances in spatial discretization on a sphere (Lecoanet *et al.* 2019; Vasil *et al.* 2019). An early precursor of the present work is the paper by Matsuda & Takayama (1989), where a dry geostrophic adjustment of localized perturbations on a sphere was studied, and differences between equatorial and midlatitude adjustments, as well as the dependence of the results on the aspect ratio, were discussed. We should emphasize that by no means the mcRSW models give a full picture of the atmospheric motions, but only their vertically averaged large-scale rudimentary-thermodynamics imprint. Shallow-water-type models with more detailed representation of thermodynamical processes in the atmosphere exist, e.g. Yano & Emanuel (1991). We, however, concentrate below on the dynamical aspects, and mcRSW models are sufficient for these purposes.

The paper is organized as follows. We briefly describe the mcRSW model and the set-up of numerical simulations in § 2. We benchmark our simulations against the previous results on the equatorial beta-plane and pinpoint key differences between spherical and beta-plane simulations with the one-layer version of the model in § 3. The same is done with the two-layer version in § 4. New results on the interactions of the equatorial modons with equatorial waves are presented in § 5. We summarize the results and discuss their possible implications for the dynamics of the tropical atmosphere in § 6.

2. The model and the set-up of numerical experiments

2.1. *The model*

The full nonlinear shallow-water systems arise upon vertical averaging of the primitive equations between pairs of material surfaces, and applying the columnar motion hypothesis, together with horizontal homogeneity of potential temperature θ (e.g. Zeitlin 2018). (The latter hypothesis can be relaxed (Kurganov, Liu & Zeitlin 2020), but we will not do it in what follows). A formulation of the primitive equations with the help of pseudo-height isobaric coordinates in the vertical (Hoskins & Bretherton 1972) is used for

this purpose. We work with a two-layer representation of the troposphere and its one-layer reduction, when the upper-layer thickness is large, and employ a free surface (a constant geopotential surface) lower boundary, representing the planetary surface, and a rigid-lid (a constant pressure surface) upper boundary representing the tropopause. We can also relax the rigid-lid upper-boundary condition and study the $2\frac{1}{2}$-layer shallow-water system (Lambaerts *et al.* 2011), which yields similar results as the two-layer system and will not be discussed below. One of the advantages of shallow-water models is that inclusion of surface topography is straightforward and computationally friendly. Studying topographic effects is, however, beyond the scope of the present study, and topography will not be incorporated in the model, which is, therefore, of the aqua-planet type.

The major difference between the moist-convective and the standard ('dry') shallow-water systems is the inclusion of a water vapour variable, with a source and a sink due to phase transitions of water, i.e. condensation and vaporization. For simplicity, the humidity will be considered below to be non-zero only in the lower layer, and close to saturation, which allows to neglect vaporization, as in Lambaerts *et al.* (2011). The latent heat release due to condensation induces upward convective fluxes and, thus, mass exchange between the two layers. In turn, the mass exchange induces a Rayleigh drag and related momentum exchanges. In the absence of dissipation the system of governing equations is written following Lambaerts *et al.* (2011), with some additions which are explained below:

$$\frac{\mathrm{d}\boldsymbol{v}_1}{\mathrm{d}t} + f\hat{k} \times \boldsymbol{v}_1 = -\boldsymbol{\nabla}(g_{11}h_1 + g_{12}h_2) \tag{2.1a}$$

$$\frac{\mathrm{d}\boldsymbol{v}_2}{\mathrm{d}t} + f\hat{k} \times \boldsymbol{v}_2 = -\boldsymbol{\nabla}(g_{21}h_1 + g_{22}h_2) + \frac{\boldsymbol{v}_1 - \boldsymbol{v}_2}{h_2}\chi\mathcal{C} \tag{2.1b}$$

$$\frac{\partial h_1}{\partial t} + \boldsymbol{\nabla} \cdot (\boldsymbol{v}_1 h_1) = -\chi\mathcal{C} \tag{2.1c}$$

$$\frac{\partial h_2}{\partial t} + \boldsymbol{\nabla} \cdot (\boldsymbol{v}_2 h_2) = +\chi\mathcal{C} \tag{2.1d}$$

$$\frac{\partial Q_1}{\partial t} + \boldsymbol{\nabla} \cdot (\boldsymbol{v}_1 Q_1) = -\mathcal{C} + \mathcal{E}. \tag{2.1e}$$

Here the subscripts 1 and 2 denote lower and upper layer, respectively. $\boldsymbol{v}_i = (u_i, v_i)$ is the horizontal velocity field in layer $i = 1,\ 2$, h_i is the thickness of layer i with values at rest H_i, f is the Coriolis parameter and Q_1 is specific humidity integrated over the air column in the moist lower layer. It can be represented as $q_1 h_1$ in terms of the mean specific humidity q_1 and lower-layer thickness h_1. Here $\mathcal{C}$ denotes condensation, which provides a sink of Q_1 and, with proportionality χ, a sink of h_1. Compared with Lambaerts *et al.* (2011), we added a surface evaporation source of moisture, $\mathcal{E}$, in the lower layer in (2.1*e*), which is the only influence of the boundary layer we include. More sophisticated parameterizations of the boundary layer can be incorporated in the model, following e.g. Schecter & Dunkerton (2009), which we do not do, for simplicity. We also keep in (2.1*a*)–(2.1*e*) the possibility to treat the $2\frac{1}{2}$-layer system with an infinite extra layer (layer 3), and a free upper surface, which corresponds to the following choice of g_{ij}:

$$\begin{bmatrix} g_{11} & g_{12} \\ g_{21} & g_{22} \end{bmatrix} = g \begin{bmatrix} 1 - \dfrac{\theta_1}{\theta_3} & 1 - \dfrac{\theta_2}{\theta_3} \\ 1 - \dfrac{\theta_2}{\theta_3} & \dfrac{\theta_2}{\theta_1}\left(1 - \dfrac{\theta_2}{\theta_3}\right) \end{bmatrix}, \tag{2.2}$$

where θ_i is the potential temperature for the i-th layer, counting from bottom. The limit $\theta_3 \to \infty$ gives a two-layer system with a rigid-lid upper boundary, which will be studied below:

$$\begin{bmatrix} g_{11} & g_{12} \\ g_{21} & g_{22} \end{bmatrix} = \begin{bmatrix} 1 & 1 \\ 1 & \dfrac{\theta_2}{\theta_1} \end{bmatrix}. \tag{2.3}$$

As in the previous works on mcRSW, a relaxational parameterization is used for condensation

$$\mathcal{C} = \frac{Q_1 - Q_s}{\tau_C}\mathcal{H}(Q_1 - Q_s), \tag{2.4}$$

where $\mathcal{H}$ denotes the Heaviside function, Q_s is the saturation value of bulk humidity, and τ_C is the relaxation time scale of over-saturation, which is short in the equatorial atmosphere, our primary concern, and is a couple of hours. One can take $Q_s = h_1 q_s$ with q_s being the vertically averaged saturation specific humidity, which depends on h_1 according to the Clausius–Clapeyron law. However, Muller *et al.* (2009) pointed out that the condensation threshold of water vapour actually scales with the saturation humidity in the boundary layer. From this viewpoint, and within the accuracy of the model, we can simply set Q_s to be constant, which we do in what follows.

The parameter χ is the coefficient linking the moisture sink to the convective mass sink, under assumption that the background stratification is moist-neutral, (cf. Bouchut *et al.* 2009; Lambaerts *et al.* 2011). The bulk formula, which is standard in modelling ocean-atmosphere exchanges (Katsaros 2001), is used for evaporation:

$$\mathcal{E} = \frac{|\boldsymbol{v}_1|}{|\bar{V}|}\frac{(Q_s - Q_1)}{\tau_E}\mathcal{H}(Q_s - Q_1), \tag{2.5}$$

where τ_E is the relaxation time scale of evaporation, which is typically on the order of a planetary day. The evaporation threshold, in principle, differs from the condensation one Q_s, but we take them to be equal, for simplicity. Note that the velocity in this formula is normalized by some fixed value $|\bar{V}|$, taken to be the maximum flow speed in the simulations below.

We can set $\chi = 1$ by simply redefining moisture variables. Defining $\tilde{Q}_1 = \chi Q_1$, $\tilde{Q}_s = \chi Q_s$, the mass and moisture equations become

$$\frac{\partial h_1}{\partial t} + \nabla \cdot (\boldsymbol{v}_1 h_1) = -\tilde{\mathcal{C}} \tag{2.6}$$

$$\frac{\partial h_2}{\partial t} + \nabla \cdot (\boldsymbol{v}_2 h_2) = \tilde{\mathcal{C}} \tag{2.7}$$

$$\frac{\partial}{\partial t}\tilde{Q}_1 + \nabla \cdot (\boldsymbol{v}_1 \tilde{Q}_1) = -\tilde{\mathcal{C}} + \tilde{\mathcal{E}} \tag{2.8}$$

$$\tilde{\mathcal{C}} = \frac{\tilde{Q}_1 - \tilde{Q}_s}{\tau_C}\mathcal{H}(\tilde{Q}_1 - \tilde{Q}_s) \tag{2.9}$$

$$\tilde{\mathcal{E}} = \frac{|\boldsymbol{v}_1|}{|\bar{V}|}\frac{\tilde{Q}_s - \tilde{Q}_1}{\tau_E}\mathcal{H}(\tilde{Q}_s - \tilde{Q}_1), \tag{2.10}$$

where $\tilde{\mathcal{C}} = \chi\mathcal{C}$, $\tilde{\mathcal{E}} = \chi\mathcal{E}$, and we set $\tilde{Q}_s = \text{const}$.

We should emphasize that in this simplest version of the model, the condensed water vapour drops off from the system, and in this sense condensation and precipitation

τ_E	τ_C	$\frac{1}{R_\beta}$	$\delta = \frac{H_1}{H_2}$
1 day	5 min	2/3/5	0.2/1.0

Table 1. Key parameter values in the numerical simulations. The moist process time scales τ_E, τ_C are given in units of planetary day. The evaporation time scale is chosen on the basis of observations, $\tau_E \sim O(1)$. Here $\tau_E \gg \tau_C =$ few time steps, with time step being one minute in our simulations; varying it moderately does not change qualitatively our conclusions. The Rossby deformation radius R_β is chosen to match the observational range, i.e. $a \cdot R_\beta \sim O(1000$ Km) (a is planetary radius).

are synonymous. (We should, probably, add at this point that a similar evolution equation for moisture was used in the early days of general circulation models, where a similar moist-convective adjustment was considered, cf. Manabe, Smagorinsky & Strickler 1965). Liquid water can be incorporated in the model along the same lines as water vapour, with similar relaxational parameterizations for its phase transitions and 'true' condensation, leading to an 'improved' mcRSW model (Rostami & Zeitlin 2018), which we will not use, keeping the number of dynamical variables and adjustable parameters minimal.

The dissipationless system (2.1*a*)–(2.1*e*), in the absence of $\mathcal{E}$, conserves total mass and momentum, and has a correct energy balance, taking into account the condensation (Lambaerts *et al.* 2011). The moist enthalpy of the lower layer $m = h_1 - \chi Q_1 \equiv h_1 - \tilde{Q}_1$ is conserved in the absence of $\mathcal{E}$ and should remain positive, by thermodynamic reasons, which provides an important constraint. The masses of individual layers are not conserved, due to the convective fluxes. The simplest way to counter-balance the loss of mass in the lower layer is to include in the right-hand side of (2.1*c*) the radiative relaxation of the form $-((h_i - H_i)/\tau_R)$, with a relaxation time τ_R, and equilibrium thickness profile H_i. A more sophisticated way to do this, is to include a large-scale descent $\mathcal{R}$ and a related drag, cf.

Randall (2015). Here we simply add $-((h_1 - H_1)/\tau_R)$ with $\tau_R = 30$ days. However, the results with and without this correction are qualitatively similar – see below.

2.2. *The set-up of numerical experiments*

The two-layer model is calibrated in a manner such that its equatorial Rossby deformation radius $R_\beta = (\sqrt{g'H_e}/2\Omega a)^{1/2}$ corresponds approximately to the observed first baroclinic equatorial Rossby deformation radius, i.e. $a \cdot R_\beta \sim O(1000$ km). Here a is the planetary radius, Ω is the angular velocity of the planet, and $H_e = (1/H_1 + 1/H_2)^{-1}$ is the equivalent depth of the two-layer model (Flierl 1978). The reduced gravity $g' = ((\theta_2 - \theta_1)/\theta_1)g$ is determined from the background 'dry' stratification θ_2/θ_1, which is taken to be 1.1 in what follows. The value of H_e can be deduced from R_β. We will explore the cases $R_\beta = 1/5, 1/3, 1/2$, dimensionally corresponding to $a \cdot R_\beta \sim O(1000$ km). The non-perturbed layer depths are $H_1 = H_e(1 + \delta)$ and $H_2 = H_e((1 + \delta)/\delta)$, where $\delta = H_1/H_2$ is the thickness ratio. We examine two cases $\delta = 1$ and $\delta = 0.2$ in the two-layer system. If we focus on the lower troposphere, we can reduce the system to one layer by keeping only the lower-layer equations. Correspondingly, the one-layer system is calibrated by setting $R_\beta = (\sqrt{gH}/\beta a)^{1/2} \in \{1/5, 1/3, 1/2\}$, where H is the non-perturbed layer depth and β is the meridional derivative of the Coriolis parameter f. The condensation relaxation time τ_C is short, as already said, and will be taken to be a couple of time steps of the numerical scheme. That is, we are close to the limit of immediate relaxation, or of strict quasi-equilibrium. See table 1 for the list of parameters.

§	$\tilde{Q}_0$	$\tilde{Q}_s$	Initial height anomaly h'/H
§ 3.2	0	—	α-Gaussian, $r_{as} \in \{1, 2\}$, $L_h/a = 1 \times R_\beta$
§ 3.3	$0.99\tilde{Q}_s$	$0.9H$	α-Gaussian, $r_{as} \in \{1, 2\}$, $L_h/a = 1 \times R_\beta$
§ 3.5	$0.99\tilde{Q}_s$	$0.7/\,0.8/\,0.9 \times H$	α-Gaussian, $r_{as} = 1$, $L_h/a = 1 \times R_\beta$
§ 5.2	Gaussian, (5.1)	$0.9H$	α-Gaussian, $r_{as} = 1$, $L_h/a = 2 \times R_\beta$

Table 2. Typical initial perturbation and background moisture field in one-layer runs. Two-layer runs have a similar set-up.

In the adjustment experiments, initial conditions are constructed by imposing onto the state of rest a circular cyclonic perturbation h, with a characteristic scale L_h and of the same α-Gaussian form as used in Rostami & Zeitlin (2019*b*), while the full thickness was corrected by a constant to maintain the global mean. Initial Gaussian perturbations $\exp(-r^2/2L_h^2)$, where r denotes the great circle distance from the reference point, yielded qualitatively similar results. We do not impose initial perturbations in velocity and moisture fields. For reader's convenience, we document here the α-Gaussian initial height anomalies $h' = h - H$,

$$h'(\tilde{r}) = \frac{\hat{h}H}{s}\sqrt{2\mathrm{e}}2^{1/s}\Gamma\left(\frac{1}{s}+\frac{1}{2}\right)G\left(\tilde{r}^s/2, \frac{1}{s}+\frac{1}{2}\right), \tag{2.11}$$

where parameter $\hat{h}$ controls the perturbation amplitude h'/H, parameter s controls the profile steepness (we fix $s = 6$ in all runs shown below as varying s does not change our conclusion qualitatively), $\Gamma(x)$ is the Gamma function and

$$G(x, y) = \frac{1}{\Gamma(y)}\int_x^y \mathrm{e}^{-t}t^{y-1}\,\mathrm{d}t \tag{2.12}$$

whose first argument is the normalized spherical distance

$$\tilde{r} = \mathcal{D}(0, 0, \lambda/r_{as}, \phi)/L_h, \tag{2.13}$$

where L_h determines the perturbation size, r_{as} controls the aspect ratio, and $\mathcal{D}(\mathrm{lat}_0, \mathrm{lon}_0, \mathrm{lat}, \mathrm{lon})$ is the great circle distance between the reference point $(\mathrm{lat}_0, \mathrm{lon}_0)$ and an arbitrary point (lat, lon) calculated with the Haversine formula.

In the benchmark experiments, the barotropic modon's stream function and its velocity, as given by Yano & Tribbia (2017), were used to initialize the thickness and the velocity fields.

In most of the simulations presented below, the initial water vapour field is chosen to be uniform and close to the saturation value, $\tilde{Q}_0 = 0.99\,\tilde{Q}_s$. We also performed simulations with variable background moisture in § 5.2, in order to represent an oceanic warm-pool. As mentioned above, $\tilde{Q}_s$ is set to be a constant. We typically set $\tilde{Q}_s = 0.9H$ ($0.9H_1$ in the two-layer model) but we examine the sensitivity of our conclusions to different choices of $\tilde{Q}_s$ in §§ 3.5 and 4. Table 2 summarizes the initial conditions for typical one-layer simulations, similar for two-layer simulations.

Numerical experiments were performed with the Dedalus algorithm developed recently (Lecoanet *et al.* 2019; Vasil *et al.* 2019). The algorithm uses spin-weighted spherical harmonics in the angular directions and rescaled Jacobi polynomials in the radial direction. For problems on the sphere, as in this study, spin-weighted harmonics allow derivative

operators to act as wavenumber multiplications on a set of spectral coefficients, in much the same way as Fourier transformation turns derivatives into wavenumber multiplications. The algorithm uses Gaussian quadrature to transform between the spectral coefficient space and the grid space, with nonlinear multiplications calculated in the grid space. We use 512 and 256 modes in the longitudinal and latitudinal directions. With a 3/2 dealias scale, this amounts to 768 longitudinal points at each latitude and 384 latitudinal points at each longitude when transferred to grid space (Vasil *et al.* 2019), i.e. a resolution of $\sim 0.5^\circ$. We checked that doubling the resolution does not change our results. No artificial viscosity/diffusivity was used in the simulations presented below. The simulations with switched-off condensation and evaporation and, thus, humidity behaving as a passive scalar, would be called 'dry' in what follows. In the opposite case, they will be called 'moist-convective', or simply 'moist'.

3. Equatorial adjustment, formation and properties of equatorial modons in one-layer RSW on a sphere as compared to the equatorial beta-plane

3.1. *Existence and stability of equatorial modons*

First, we benchmarked our numerical scheme and, at the same time, cross-checked the results of Yano & Tribbia (2017) by initializing the dry one-layer simulations with a modon solution of the barotropic model on the sphere. The construction of this solution followed Tribbia (1984) and Yano & Tribbia (2017). As the result, we got long-lasting shallow-water modons even without imposing a nonlinear normal-mode balance condition, which was done in Yano & Tribbia (2017). Our results are similar for different R_β values, and we present here the case of $R_\beta = 1/2$. There are two free parameters which define the barotropic modon solution: the phase speed C_p and the angular size parameter ϕ_0. Figure 1 shows the evolution of the initial barotropic modon with the phase speed $C_p \approx 12$ m s^{-1} and the size parameter $\phi_0 = 10^\circ$. The shallow-water modon propagates eastward steadily with approximately its assigned phase speed (12 m s^{-1}, which is $\sim 10^\circ$/day), and experiences no obvious dissipation until $t = 35$ days (inertia-gravity waves become more visible afterwards). This confirms the existence of equatorial modon solutions in shallow-water systems on the rotating sphere, and their stability. One can vary the phase speed and the size parameter independently to obtain a modon solution; however, not all combinations of C_p and ϕ_0 yield stable shallow-water modons. Yano & Tribbia (2017) gave a survey on stability of modon solutions in the phase space spanned by C_p and ϕ_0, but we will not go further in that direction, as our main focus below is on generation of modons from 'unprepared' initial perturbations.

3.2. *Dry equatorial adjustment*

We then performed one-layer dry adjustment experiments in order to benchmark equatorial adjustment process on the sphere. In the midlatitude geostrophic adjustment problem, it is known that the pressure (velocity) field adjusts to be in equilibrium with the velocity (pressure) field when the perturbation scale is smaller (larger) than the midlatitude deformation radius. Matsuda & Takayama (1989) found that a similar rule holds in equatorial adjustment processes on the sphere. We thus compare in figure 2 equatorial adjustment processes with different initial perturbation scales L_h, all other parameters being the same. The initial stages of the adjustment process turned out to be rather insensitive to the initial perturbation amplitude and we only show results for the case with $h'/H = 0.1$ in this subsection. We first note that, as found in Matsuda & Takayama (1989),

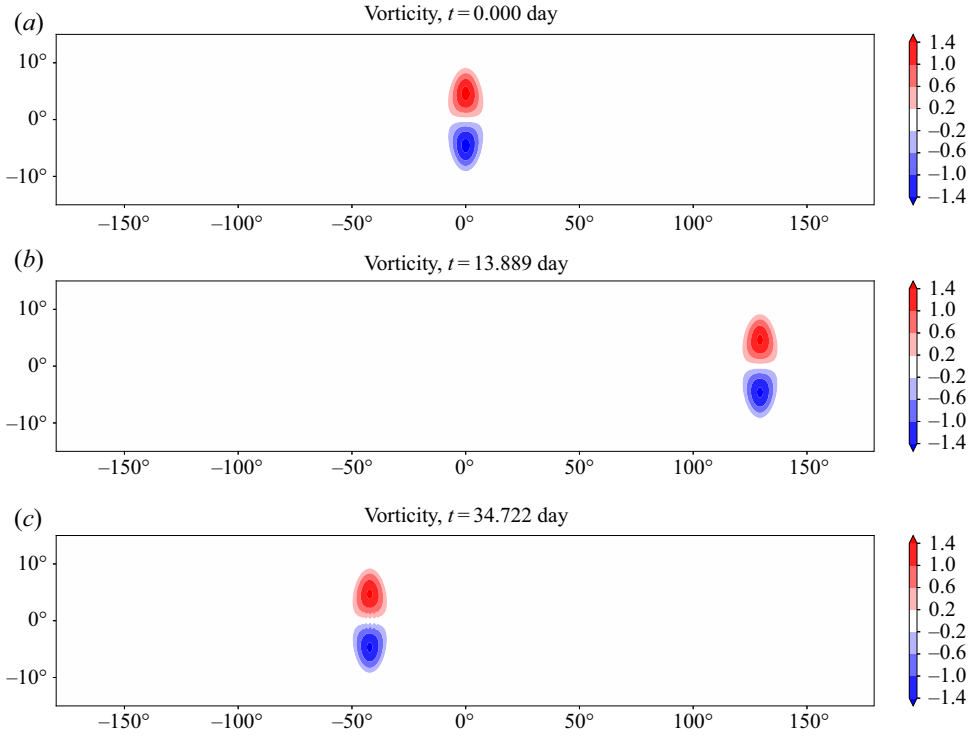

Figure 1. Evolution of the initial configuration corresponding to a barotropic modon with parameters $C_p \approx 12$ m s^{-1} and $\phi_0 = 10^\circ$, as follows from dry simulations with the one-layer RSW model on a sphere. Relative vorticity is shown in colours. In this and subsequent figures, time is measured in units of planetary day.

the equatorial adjustment process is dominated by equatorial Kelvin and Rossby waves when $L_h/a > R_\beta$ while inertia-gravity waves are more visible when $L_h/a < R_\beta$. As is well-known, the short inertia-gravity waves are close to pure gravity waves, with isotropic propagation properties. Consistently, the feature of isotropic propagation is clearly visible in the case of $L_h/a = 0.5 \times R_\beta$. In the case of $L_h/a = R_\beta$, four classical species of equatorial waves (e.g. Matsuno 1966) are clearly distinguishable: the Kelvin wave ($\sim 60^\circ$ longitude), the $n = 1$ eastward-propagating inertia-gravity wave ($\sim 30^\circ$ longitude), the $n = 1$ Rossby wave $\sim -10^\circ$ longitude and the $n = 1$ westward-propagating inertia-gravity wave ($\sim -50^\circ$ longitude). Note that our choice of initial perturbation being symmetric with respect to the equator excludes anti-symmetric Yanai waves and even-n Rossby and inertia-gravity waves. To summarize, as the perturbation size L_h increases with respect to the deformation radius, the inertia-gravity wave field changes, such that its anisotropy increases, and its amplitude, relative to the Kelvin and Rossby waves, decreases.

Rostami & Zeitlin (2019*a*) compared, on the equatorial beta-plane, the process of adjustment of perturbations with different aspect ratios (zonal-to-meridional) to examine the often assumed long-wave limit corresponding to perturbations with a large aspect ratio in the initial value problem. At large aspect ratios, they confirmed theoretical predictions of Le Sommer, Reznik & Zeitlin (2004), and found that the adjustment mostly results in equatorial Kelvin and Rossby waves; while at order-one aspect ratios a significant part of response to the west of the perturbation consisted in long westward-propagating inertia-gravity waves. In figure 3, we present the results of simulations of the adjustment process on the sphere with different aspect ratios of initial perturbation. The initial

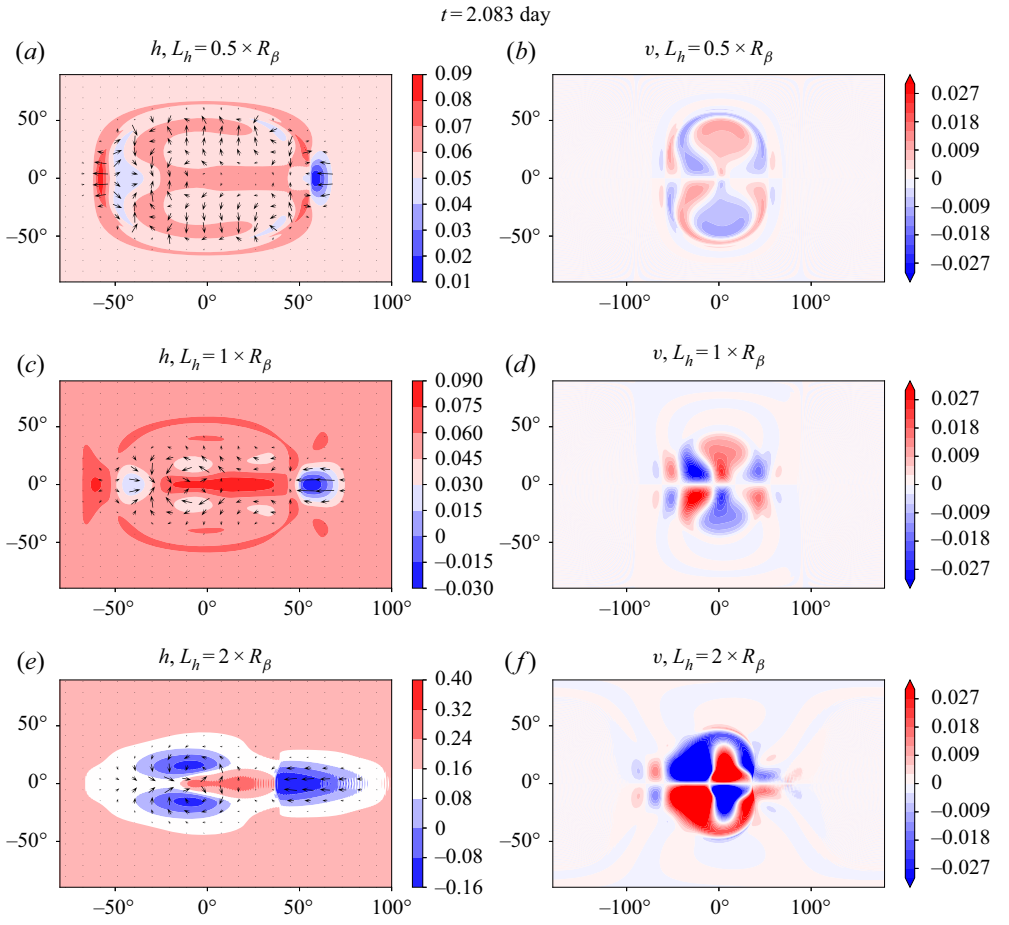

Figure 2. (*a–f*) snapshots of thickness anomaly $h' = h - H$ with superimposed velocity arrows (*a*,*c*,*e*) and meridional velocity (*b*,*d*,*f*) for initial height perturbations with size $0.5 \times aR_\beta$, $1 \times aR_\beta$ and $2 \times aR_\beta$, respectively. Dry adjustment in the one-layer model with $R_\beta = 1/5$ and initial perturbation of aspect ratio 1 and amplitude $h'/H = 0.1$. The Kelvin wave needs 12.5 days to travel around the equator for $R_\beta = 1/5$.

perturbations of zonal-to-meridional aspect ratio 1 or 2 (i.e. $r_{as} = 1$ or 2 in (2.13)) were imposed on the equator at 0° longitude. Let us first examine the case with $R_\beta = 1/2$ figure 3(*a*,*b*), in order to compare with Rostami & Zeitlin (2019*a*). The Kelvin wave at ∼150° longitude, the $n = 1$ Rossby wave at ∼0° longitude and the $n = 1$ westward-propagating inertia-gravity wave at $\sim -100°$ longitude are clearly visible in pressure and velocity fields for perturbation of aspect ratio 1. In contrast, the $n = 1$ westward-propagating inertia-gravity wave is no longer visible for perturbation of aspect ratio 2, so the equatorial Kelvin and Rossby waves dominate the adjustment process. A similar scenario is realized in the case of $R_\beta = 1/5$, except that the whole wave field is smaller in scale, due to the smaller R_β. It thus seems that as the initial perturbation elongates zonally, so do the Kelvin and Rossby waves, leaving less space for inertia-gravity waves. Below we will focus on the results with initial perturbations with an aspect ratio of 1 and size $1 \times aR_\beta$.

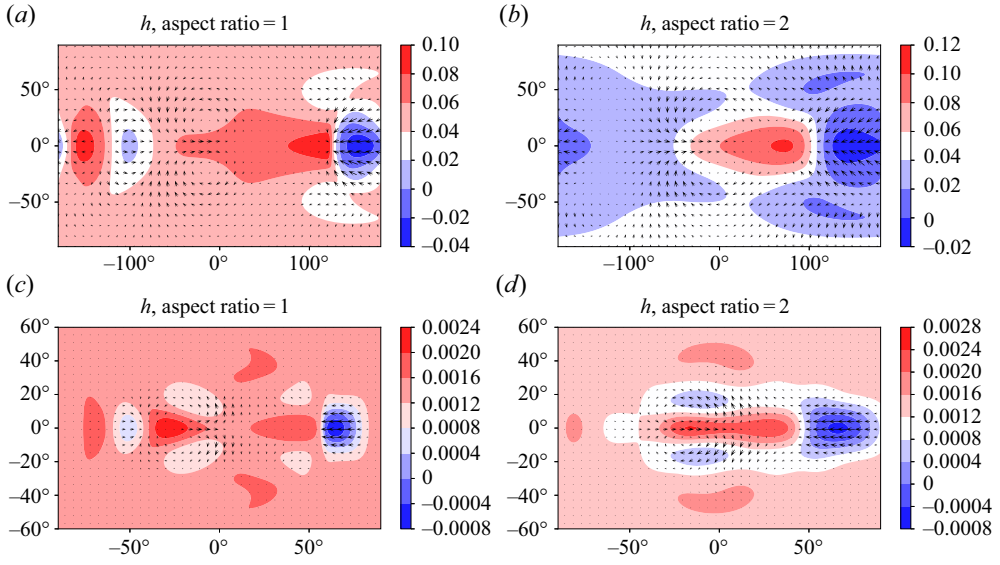

Figure 3. Snapshots of thickness anomaly (colours) and velocity (arrows) during evolution of initial height perturbations of aspect ratio 1 (*a*,*c*) and aspect ratio 2 (*b*,*d*). In panels (*a*,*b*), $R_\beta = 1/2$ and $t = 0.833$ days. In panels (*c*,*d*) $R_\beta = 1/5$ and $t = 2.361$ days. Dry adjustment in the one-layer model with initial perturbation amplitude $h'/H = 0.1$. The Kelvin wave needs 2 and 12.5 days to travel around the equator for $R_\beta = 1/2$ and $R_\beta = 1/5$, respectively. Note that the latitude/longitude range differs between the top and the bottom rows.

3.3. *Dry vs moist-convective adjustment*

We then compare the equatorial adjustment processes in the one-layer model in dry and moist-convective configurations, with the same initial perturbation of thickness. A zoom of the results is shown in figures 4 and 5 for the case of $R_\beta = 1/5$ and initial perturbation amplitude $h'/H = 0.15$. Varying R_β or initial perturbation amplitude does not significantly modify the early stages of the adjustment process, but does lead to differences in the long-term evolution (see below). The adjustment process in the dry case generates familiar equatorial waves. Following initial convergence, the Kelvin wave propagates eastward steadily with the characteristic phase speed, $\sqrt{gH}$ while Rossby waves are left behind, having smaller westward phase speeds. The $n = 1$ Rossby wave is clearly seen in the vorticity field in figure 5(*a–d*) around 0°. However, when moist convection is turned on, we observe the familiar chevron pattern which was found by Gill (1980) as a steady solution of the forced linear problem, and became foundational in tropical meteorology and climatology. Specifically, the Kelvin wave does not detach until $t = 1.319$ days while the Rossby wave evolves into a compact cyclone pair characterized by closed contours of constant h (figure 4) and strong vorticity (figure 5).

We note that condensation regions practically coincide with (moisture) convergence areas, where $\boldsymbol{\nabla} \cdot \boldsymbol{v} < 0$ (figure 5), while evaporation is approximately an order of magnitude smaller than condensation, implying that condensation is driven by dynamics rather than by local evaporation anomalies. Initially, convergence takes place in the centre of the negative pressure anomaly. As the Kelvin and Rossby waves develop, convergence concentrates around the Rossby lobes, in the westward-propagating inertia-gravity wave packet, and at the rear of the Kelvin wave (the dispersionless Kelvin wave of depression steepens there, cf. e.g. Le Sommer *et al.* 2004). Formation of cyclonic pairs by Rossby waves apparently results from positive feedbacks associated with the moist processes:

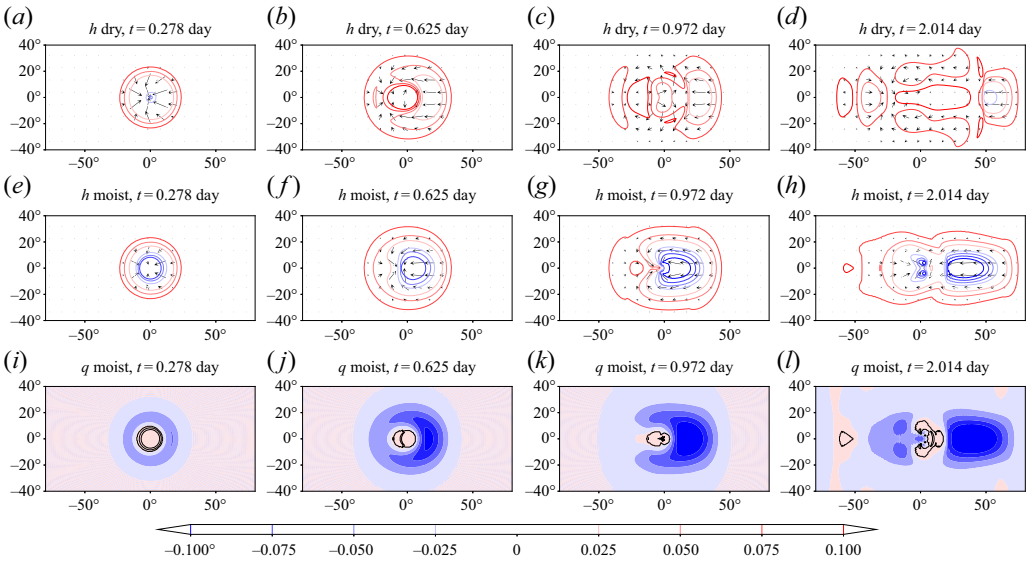

Figure 4. Comparison of equatorial adjustment processes in the dry (*a–d*) and moist-convective (*e–h*, *i–l*) one-layer shallow-water systems on the sphere at early stages. Non-dimensional thickness anomaly h'/H (colours) and velocities (arrows) are shown in panels (*a–d*) and (*e–h*). Perturbation moisture $\tilde{Q}'$, normalized by saturation value $\tilde{Q}_s$, is shown in the bottom row with black contours enclosing condensation regions. Here $R_\beta = 1/5$, and initial perturbation amplitude $h'/H = 0.15$. The dry and moist Kelvin waves need 12.5 and 15–17 days, respectively, to travel around the equator with $R_\beta = 1/5$.

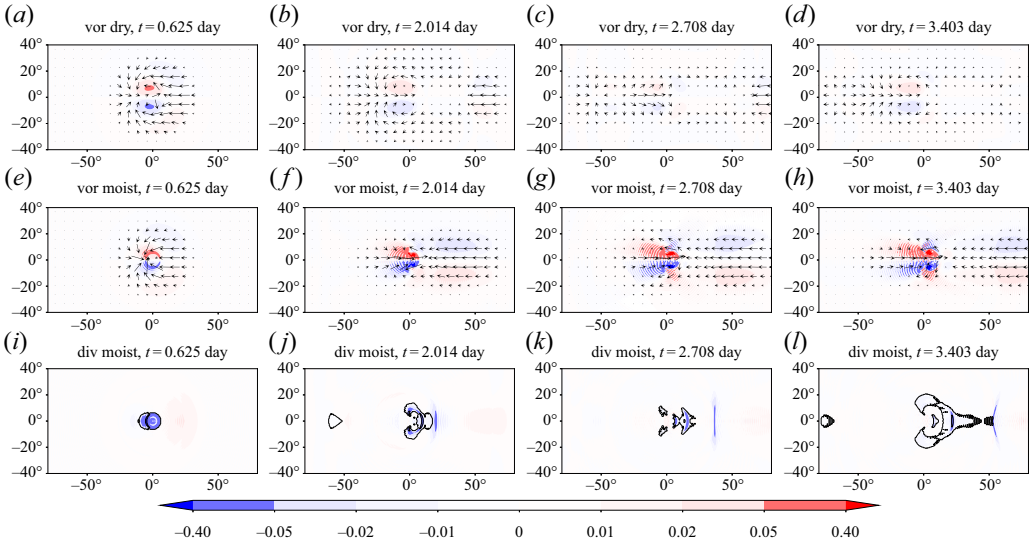

Figure 5. Same as in figure 4, but for relative vorticity (*a–d*, *e–h*) and divergence $\nabla \cdot \boldsymbol{v}$ (*i–l*). Colour scheme is saturated at large values.

moisture convergence accompanying Rossby lobes triggers condensation and associated convective updraught (figure 5), yielding even lower h and more moisture convergence. Or, equivalently, latent heat release/convective updraughts enhance convergence and, hence, relative vorticity via the conservation of angular momentum.

We thus see that adjustment in the moist-convective one-layer system exhibits a Gill pattern. Yet the simulated Gill pattern is only a transient feature such that the Kelvin wave and the cyclone pair separate subsequently due to a difference in phase speeds. The situation is, thus, similar to what was observed in the adjustment experiments with one-layer mcRSW on the equatorial beta-plane by Rostami & Zeitlin (2019*b*).

Another notable feature is that the moist Kelvin wave induces a persistent zonal easterly jet resulting from the Kelvin wave breaking, as it propagates around the Equator (figure 5*e–h*). We will come back to this observation below.

3.4. *Twin cyclones vs equatorial modons*

The longer-time evolution of the aforementioned transient Gill pattern depends on the amplitude of the initial perturbation, and also on R_β. Generally speaking, while moist Kelvin waves steadily propagate eastward, Rossby waves evolve into either a pair of cyclones propagating westward and toward the pole in each hemisphere, or into a stable eastward-propagating equatorial modon, depending on the initial perturbation amplitude and deformation radius R_β. This is again consistent with what was found by Rostami & Zeitlin (2019*a*).

Figure 6 shows that the cyclonic pair generated by the adjustment process initially moves eastward with a propagation speed proportional to its intensity (figure 6*b*,*e*,*h*), consistent with an interpretation in terms of equatorial modons. The cyclone pair turns into a westward-moving Rossby-wave packet at weaker intensities (figure 6*c*) while continues moving eastward as an equatorial modon at stronger intensities (figure 6*f*,*i*). The propagation velocity of cyclonic modons in dry environment is determined by the balance between two major factors – westward tendency resulting from β-effect and eastward tendency resulting from mutual nonlinear advection within the pair of cyclones (Flierl *et al.* 1980). The stronger cyclones are, the stronger nonlinear advection effects are, and hence the greater phase speed is, and vice versa.

Note that these westward-propagating Rossby-wave packets are not Boyd's solitons (Boyd 1985). First of all, westward-propagating Rossby-wave solitons are pairs of anticyclonic vortices while the localized Rossby wave packets are 'twin cyclones'. Furthermore, Rossby-wave solitons propagate westward with phase speeds greater than linear Rossby wave phase speed due to the nonlinear interaction of the two anticyclonic vortices, while the westward propagation speed of localized Rossby-wave packets, or twin cyclones, lies well within the linear range.

In order to analyse the mechanism of the modon propagation in moist environments, we have to take into account feedbacks associated with moist convection. Shown in figure 7 is the divergence field $\nabla \cdot \boldsymbol{v}$ with black contours enclosing strong condensation regions. Similar to what was observed above in figure 5 at the early stages of adjustment, the regions of condensation coincide with strong convergence areas, suggesting a positive feedback. For weak initial perturbations (figure 6*a–c*), the pair of cyclones splits under the effect of the 'β-drift', a phenomenon that cyclones propagate towards the North-West (South-West) in the Northern (Southern) hemisphere (e.g. Sutyrin & Flierl 1994; Reznik & Grimshaw 2001). The convergence field associated with the cyclone pair then vanishes, and condensation, which helps to 'glue up' the cyclones, diminishes. Meanwhile, for sufficiently strong initial perturbations (figure 6*g–i*), strong nonlinear advection dominates the β-drift, and the cyclone pair stays compact, maintaining a steady convergence pattern, which continues to promote the cyclone growth via the positive feedback of convection. This means that a sufficiently large amplitude of the initial perturbation is required for

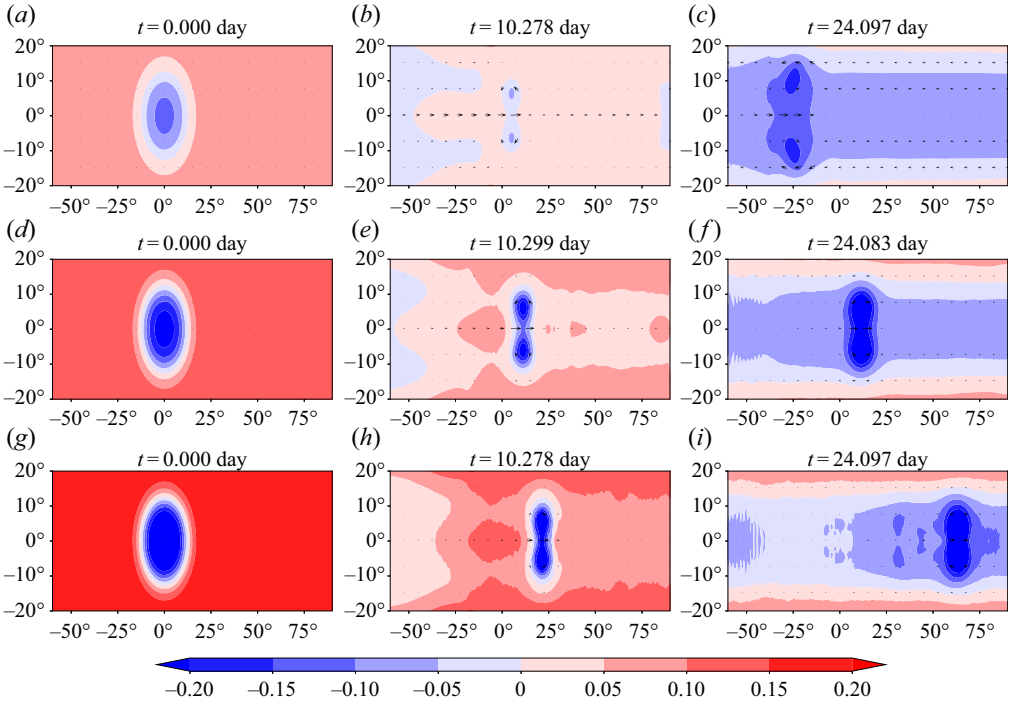

Figure 6. Comparison of later stages of the evolution of the cyclone pairs generated by the adjustment process in moist-convective environment for three different intensities of the initial perturbation, as seen in non-dimensional thickness anomaly h'/H field. The maximum amplitudes of the initial non-dimensional perturbation h'/H are $\approx$0.1 (*a–c*), 0.2 (*d–f*) and 0.3 (*g–i*), respectively. The moist Kelvin wave need 15–17 days to travel around the equator for the chosen value of the deformation radius, $R_\beta = 1/5$.

generation of coherent equatorial modons. We will show below that the eastward-moving equatorial modons could still turn into westward-moving twin cyclones after propagating eastward for tens of days, due to the influence of moist-convective Kelvin waves (§ 5.1), which need 15–17 days to make a tour around the Equator.

The emergence of equatorial modons in spherical geometry also depends on the value of the non-dimensional equatorial deformation radius R_β, which makes a difference with the equatorial beta-plane where planetary radius does not explicitly appear. For example, with initial perturbation amplitude $h'/H = 0.3$, the previous simulation with $R_\beta = 1/5$ yields steadily eastward-propagating equatorial modons (figure 6*g–i*) while simulations with $R_\beta = 1/3$ yield twin cyclones that propagate westward and poleward in each hemisphere, as follows from figure 8(*b*). A similar behaviour is observed for initial perturbation amplitude $h'/H = 0.2$, i.e. a switch from equatorial modon to twin cyclones as R_β increases from 1/5 to 1/3 (not shown). Therefore, the radius of the planet sets an upper limit on R_β for which the modon solutions are allowed.

3.5. *Sensitivity to the saturation value of bulk humidity*

As already said above, we chose an *ad hoc* value of the condensation threshold $\tilde{Q}_s = 0.9H$. In this section, we investigate the sensitivity of the previous one-layer results to this value. Shown in figure 9(*a*) is the longitudinal position of the global vorticity maximum, corresponding to the cyclone pair developed in the Rossby-wave sector. It is seen that the cyclone pair moves eastward, as an equatorial modon, when the saturation

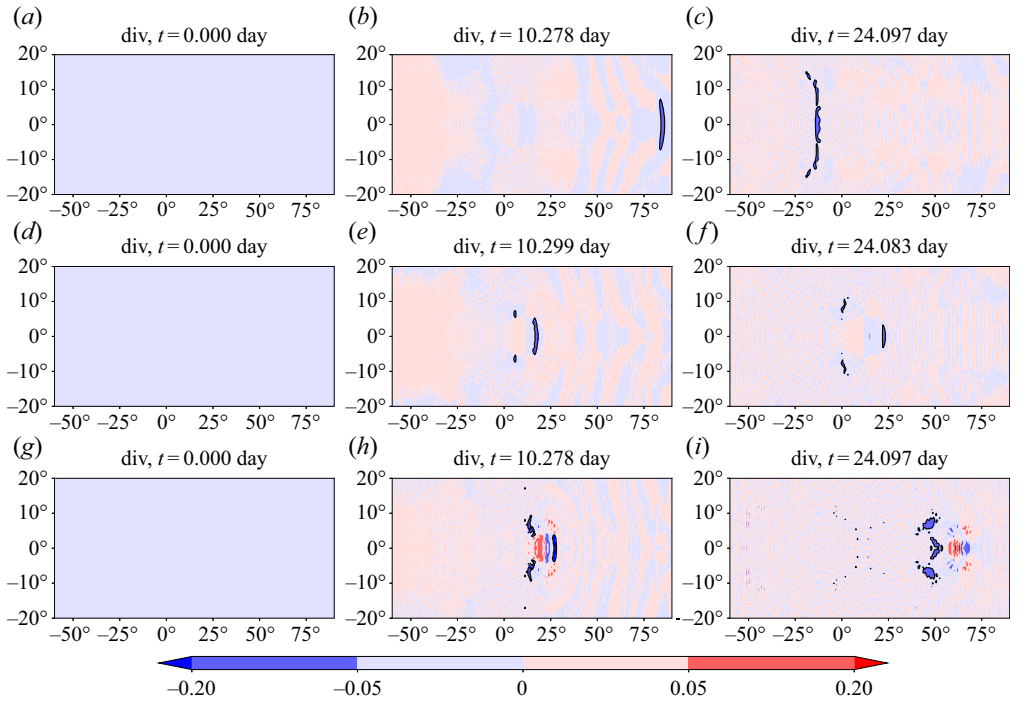

Figure 7. Same as figure 6 but for $\nabla \cdot \boldsymbol{v}$. Black contours enclose strong condensation regions, which coincide with moisture convergence areas. There is a large area of weak condensation westward of the modon, which is purposely eliminated by our choice of contour levels.

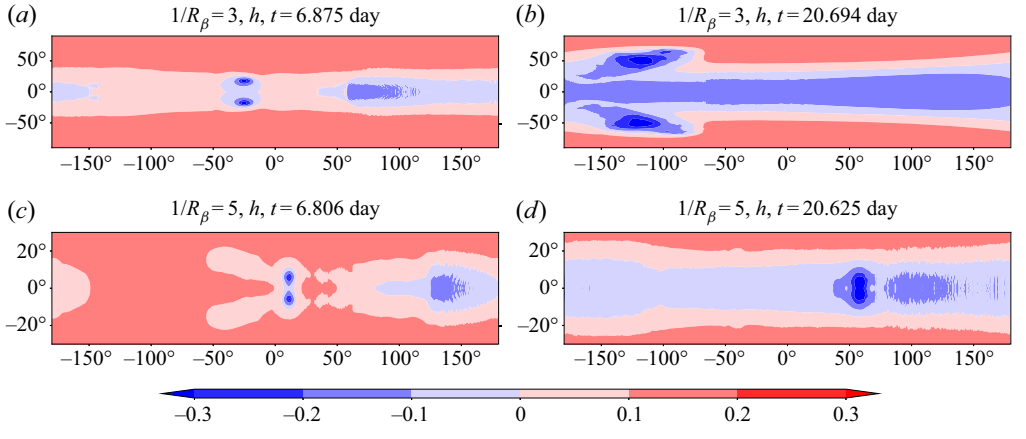

Figure 8. Comparison of the behaviour of cyclone pairs generated by the adjustment process at $R_\beta = 1/3$ (a,b) and $R_\beta = 1/5$ (c,d) at later stages, as seen in the thickness anomaly field h'/H. Note the change in latitude and longitude ranges with respect to previous figures. Maximum amplitudes of initial non-dimensional perturbation h'/H are approximately 0.3. Panels (c and d) shows the simulation of figure 6(g–i), duplicated here to facilitate the comparison.

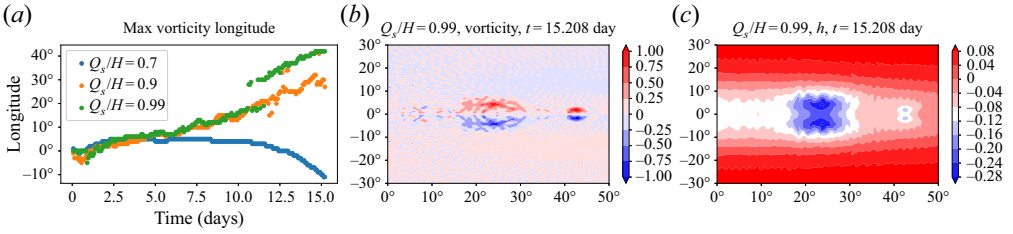

Figure 9. Comparison of the evolution of cyclone pairs for different values of bulk saturation humidity $\tilde{Q}_s/H$ (*a*), as measured by the evolution of the longitude of vorticity maximum. In all cases, $R_\beta = 1/5$ and the initial perturbation amplitude is $h'/H = 0.3$. Panels (*b*,*c*) show vorticity and thickness anomaly h'/H patterns for $\tilde{Q}_s = 0.99H$ at $t \approx 20$ days, to illustrate the discontinuity seen in the panel (*a*) (green circles). The wiggles in vorticity and thickness fields are due to the interaction of the dipole with circumnavigating Kelvin wave and related generation of small-scale inertia-gravity waves.

value of bulk humidity is sufficiently large ($\tilde{Q}_s \geqslant 0.8H$), while it quickly transforms into a westward-propagating twin-cyclone wave packet after a brief stage of eastward propagation, when the bulk saturation humidity is small. Thus, the one-layer adjustment process does exhibit a sensitivity to the value of bulk saturation humidity, while the general scenarios of adjustment remain the same as described before. Presumably, larger saturation values of bulk humidity allow for a stronger moist positive feedback, and hence favour the formation of equatorial modons.

A notable feature in figure 9 is the jump in longitude of vorticity maximum at $t \approx 10$ days when $\tilde{Q}_s = 0.99H$ (green circles). To understand the reasons for this jump, we show in figure 9(*b*,*c*) the corresponding vorticity and pressure fields at $t \approx 15$ days. One observes two distinct vorticity extrema, corresponding to two cyclonic pairs, located at approximately 20° and 40° longitude, respectively. A closer inspection of the evolution suggests that the smaller in size secondary equatorial modon to the east is induced by the original modon. The sudden jump in the global vorticity maximum which is seen in figure 9(*a*) (green circles) indicates that the vorticity signal associated with the secondary modon exceeds that of the original modon at approximately 10 days. This inductive generation of a secondary modon is discussed in detail in § 5.2 below. The noisiness in the vorticity and pressure fields in figure 9(*b*,*c*) is due to small-scale inertia-gravity waves generated by the interaction of the vortex dipole with a circumnavigating moist-convective Kelvin wave. After the interaction with the Kelvin wave, the equatorial modon actually transforms into westward-moving twin cyclones. The interaction between Kelvin waves and equatorial modons will be discussed in § 5.1.

Finally, before proceeding to two-layer results, we should emphasize that moderate variations of the stratification parameter does not change the results qualitatively (not shown).

4. Equatorial adjustment, formation and properties of equatorial modons in two-layer RSW on a sphere as compared to the equatorial beta-plane

The convective updraughts naturally induce a significant baroclinic response in the two-layer system, while the barotropic response is, comparatively, weak. Let us recall the decomposition in barotropic and baroclinic modes in linearized equations which will be used in diagnostics of numerical simulations with the two-layer model. We take the immediate relaxation limit, in the absence of evaporation $\tilde{\mathcal{E}}$, in the moisture equation (2.8),

as explained, e.g. in Rostami & Zeitlin (2020*a*),

$$\tilde{Q}_s \nabla \cdot \boldsymbol{v}_1 = -\tilde{\mathcal{C}}. \tag{4.1}$$

Then the linearized system for perturbations of velocity and thickness about the state of rest becomes

$$\frac{\partial \boldsymbol{v}_1}{\partial t} + f\hat{k} \times \boldsymbol{v}_1 = -\nabla(h_1' + h_2'), \tag{4.2a}$$

$$\frac{\partial \boldsymbol{v}_2}{\partial t} + f\hat{k} \times \boldsymbol{v}_2 = -\nabla(h_1' + s \cdot h_2'), \tag{4.2b}$$

$$\frac{\partial h_1'}{\partial t} + H_1 \nabla \cdot \boldsymbol{v}_1 = \tilde{Q}_s \nabla \cdot \boldsymbol{v}_1, \tag{4.2c}$$

$$\frac{\partial h_2'}{\partial t} + H_2 \nabla \cdot \boldsymbol{v}_2 = -\tilde{Q}_s \nabla \cdot \boldsymbol{v}_1. \tag{4.2d}$$

We define $\boldsymbol{v}_\pm = \boldsymbol{v}_1 + A_\pm \boldsymbol{v}_2$ and $h'_\pm = h'_1 + B_\pm h'_2$ to get the uncoupled system

$$\frac{\partial \boldsymbol{v}_\pm}{\partial t} + f\hat{k} \times \boldsymbol{v}_\pm = -\alpha_\pm \nabla h'_\pm, \tag{4.3a}$$

$$\frac{\partial h_\pm}{\partial t} + \gamma_\pm \nabla \cdot \boldsymbol{v}_\pm = 0, \tag{4.3b}$$

where $\alpha_\pm = 1 + A_\pm$ and $\gamma_\pm = H_1(1 + (B_\pm - 1)\tilde{Q}_s/H_1)$, while $B_\pm = ((1 + s \cdot A_\pm)/(1 + A_\pm))$. Here $A_\pm$ are the roots of the quadratic equation

$$\left(1 + (s-1)\frac{\tilde{Q}_s}{H_1}\right) A^2 + \left(1 - \frac{s}{\delta}\right) A - \frac{1}{\delta} = 0, \tag{4.4}$$

and we recall that $s = \theta_2/\theta_1$ and $\delta = H_1/H_2$. Since convection mostly affects the baroclinic mode, we will be generally presenting below the results for this mode. Notice that A_- is close to -1 with our choices of parameters.

We compare dry and moist adjustments in the two-layer model in figure 10 for the case of $\delta = 1, R_\beta = 1/5$ and initial perturbation amplitude $h_1'/H_0 = 0.075$, where $H_0 = H_1 + H_2$ is the total fluid depth. Note we only impose initial perturbation in the lower layer. We find that moist convection induces a transient Rossby-Kelvin hybrid structure similar to the one-layer system. This is reminiscent of the study of Rostami & Zeitlin (2020*a*), who reported a much longer-lasting, albeit also transient, Gill pattern in the lower-layer thickness anomaly in the two-layer shallow-water model on the equatorial beta-plane. We note that varying moderately the depth ratio δ, deformation radius R_β or initial perturbation amplitude does not qualitatively change the early stages of the adjustment process (not shown).

The long-term evolution of generated baroclinic cyclone pairs also exhibits a similar scenario as compared with the one-layer system. In particular, there exists a transition between westward-propagating twin-cyclone regime and eastward-propagating equatorial modon regime as R_β or initial perturbation amplitude varies. An additional parameter, the depth ratio $\delta = H_1/H_2$ is present in the two-layer system, and we investigated the dependence of the results on it. It turns out that smaller depth ratios δ are more favourable for generation of eastward-moving equatorial modons, given the same perturbation amplitude relative to the lower-layer depth, h_1'/H_1. This is, presumably, due to a smaller

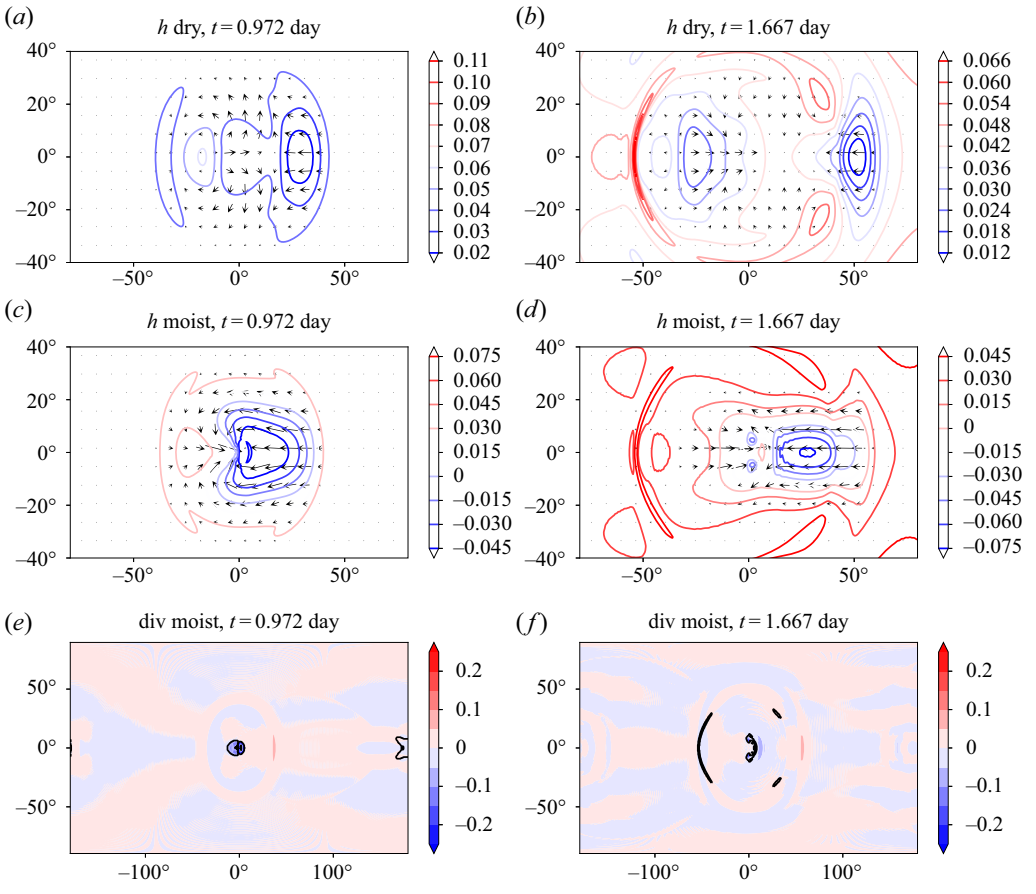

Figure 10. Two snapshots of the baroclinic mode resulting from the adjustment process in dry and moist-convective two-layer shallow-water systems. (*a–f*) Colour: non-dimensional baroclinic thickness anomaly h'_-/H_0 for the dry simulation and h'_-/H_0 and $\nabla \cdot \boldsymbol{v}_-$ for the moist simulation. Arrows: velocity field. The values of parameters are: $s = 1.1$, $\delta = 1$, $\tilde{Q}_s = 0.9H_1$, $A_+ \approx 1$, $A_- = -0.91$, $B_+ = 1.05$, $B_- = 0.05$.

upper-layer velocity, as compared with the lower-layer one, of the cyclonic pair when $\delta < 1$, which implies a weaker westward nonlinear advection tendency in the upper layer that counteracts the eastward nonlinear advection tendency in the lower layer (we recall that a strong baroclinic mode implies opposite velocities in the layers), and hence promotes an eastward-propagating baroclinic modon. We show in figure 11 an inter-comparison of cyclone pair evolution in the cases $\delta = 1$ and $\delta = 0.2$. Before proceeding, we note that in the long-term the eastward-moving baroclinic pairs arising in the simulations exhibit a reverse propagation: the eastward-propagating baroclinic modon in figure 11(*c*,*d*) changes its propagation direction after approximately 15 days. We will discuss this phenomenon in more detail in § 5.1.

In general, our results on two-layer adjustment on the sphere agree with and complement those obtained on the equatorial beta-plane in Rostami & Zeitlin (2020*a*), including the transient Gill pattern at early stages and generation of eastward-propagating baroclinic modon at later stages, when proper parameters are chosen. We should emphasize that the baroclinic moist-convective Kelvin wave induces a persistent easterly zonal jet as it propagates around the Equator (figure 11*b*,*d*). It arises due to the Kelvin wave breaking

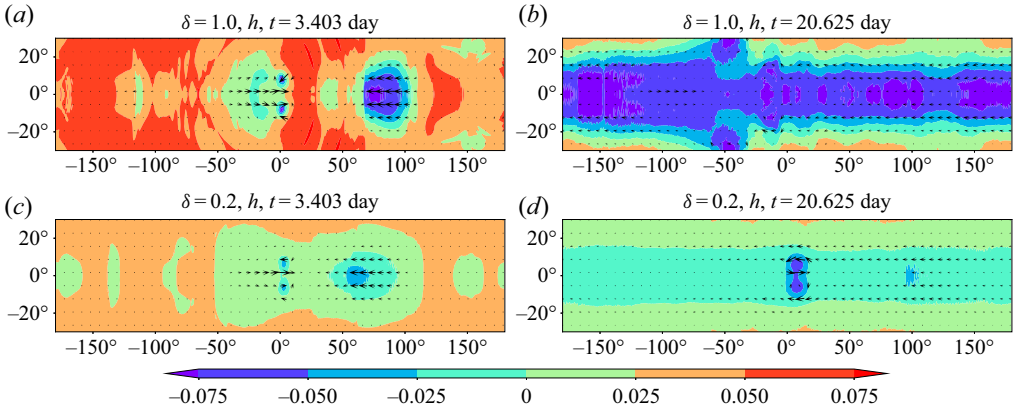

Figure 11. Two snapshots of the baroclinic mode resulting from the adjustment process in moist-convective environment in the two-layer shallow-water systems with depth ratios $\delta = 1$ (a,b) and $\delta = 0.2$ (c,d), as seen in the h'_-/H_0 field. In both cases, $R_\beta = 1/5$ and initial perturbation $h'_1/H_1 = 0.3$. Note that $h'_1/H_0 = 0.15$ when $\delta = 1$, while $h'_1/H_0 = 0.05$ when $\delta = 0.2$ (the scenario remains qualitatively the same if we take same h'_1/H_0 for both values of δ). Colours: non-dimensional baroclinic thickness anomaly h'_-/H_0. Arrows: baroclinic velocity field v_-. It takes 15–17 days for the baroclinic moist Kelvin wave to propagate around the Equator when $R_\beta = 1/5$.

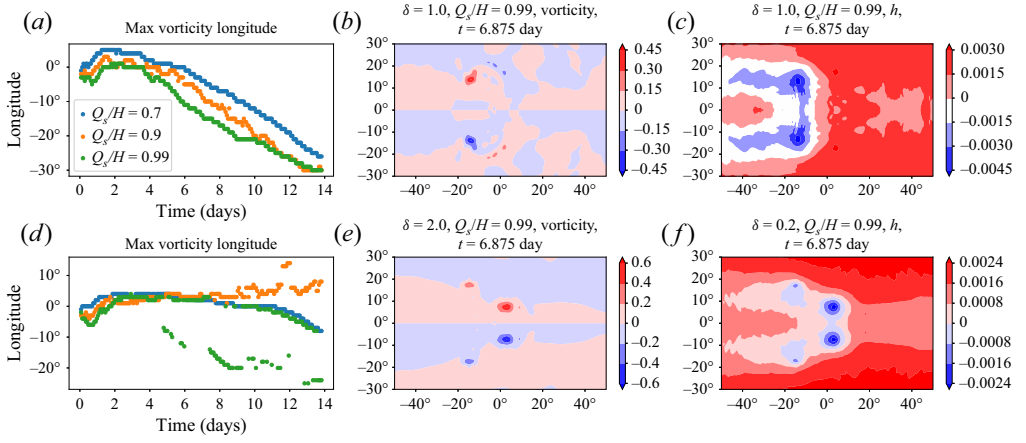

Figure 12. Comparison of the evolution of baroclinic cyclone pairs at different values of bulk saturation humidity $\tilde{Q}_s/H_1$ at $\delta = 1$ (a–c) and $\delta = 0.2$ (d–f). (a,d) Time evolution of the global maxima of the baroclinic vorticity. (b,c,e,f) Baroclinic vorticity and baroclinic thickness anomaly h'_-/H_0 fields at a chosen time. The longitude of the baroclinic cyclone pair is approximated by the longitude of baroclinic vorticity maximum. In both cases $R_\beta = 1/5$ and initial perturbation amplitudes $h'_1/H_1 = 0.3$.

and the resulting generation of potential vorticity anomaly (cf. Le Sommer *et al.* 2004). We will comment on this observation below when we discuss the interaction between the cyclone pairs and Kelvin waves.

The sensitivity of the long-term evolution of the baroclinic cyclone pairs to bulk saturation humidity value is shown in figure 12. At depth ratio $\delta = 1$ and different $\tilde{Q}_s/H_1$, the cyclone pairs quickly turn westward, becoming Rossby-wave packets, after a brief period of initial eastward propagation. When the depth ratio $\delta = 0.2$, the picture is more subtle: we get westward-moving twin cyclones up to 14 days for $\tilde{Q}_s/H_1 = 0.7$ and 0.99,

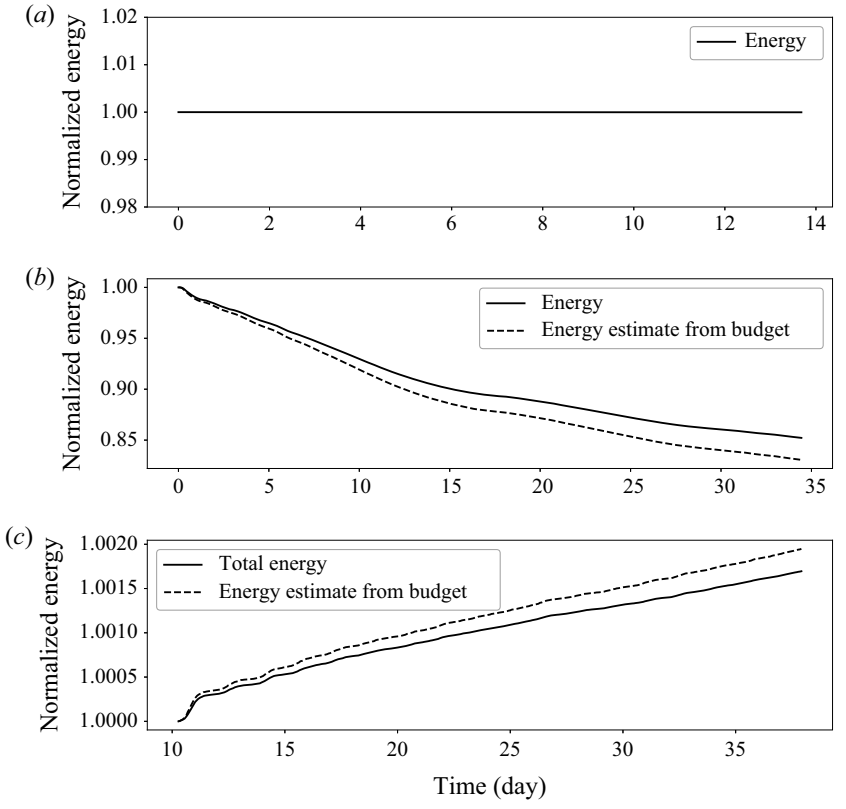

Figure 13. Energy evolution in typical simulations: one-layer dry model (*a*), one-layer moist-convective model (*b*) and two-layer moist-convective model (*c*). Black solid lines: time series of energy, normalized by the initial value, calculated from pressure and velocity fields. Black dashed lines in panels (*b*,*c*) show normalized energy evolution estimated from the theoretical energy budget. In one-layer simulations, $R_\beta = 1/5$ and initial perturbation $h'/H = 0.3$. In two-layer simulations, $R_\beta = 1/5$, $h_1'/H_0 = 0.05$

and eastward-moving modon up to 14 days for $\tilde{Q}_s/H_1 = 0.9$. However, as we will show below, even the modon generated in the case with $\tilde{Q}_s/H_1 = 0.9$ turns westward later on, under the influence of the Kelvin wave.

4.1. *Energy budget: theory vs numerical experiments*

To conclude the benchmarks and comparisons with previous results on the equatorial beta-plane, we analyse the energy budget in typical simulations. To keep the energy budget simple, we leave out the restoring term $(h_1 - H_1)/\tau_R$ that represents large-scale descent in simulations analysed in this subsection. In the one-layer dry model, the total energy $E = \int \mathrm{d}\boldsymbol{x}(|\boldsymbol{v}|^2 h + gh^2)/2$ should be conserved. The energy loss in the dry numerical simulations is, indeed, negligible, confirming reliability of the Dedalus code (cf. figure 13*a*). The one-layer moist model, however, continually loses energy with convective updrafts transporting mass and momentum out of the one-layer system:

$$\frac{\partial}{\partial t}E = -\int \mathrm{d}\boldsymbol{x}\left[\mathcal{C}\left(\frac{|\boldsymbol{v}|^2}{2} + gh\right)\right]. \tag{4.5}$$

The energy time series vs energy estimate based on the above energy budget are shown in figure 13(*b*) for the case with $R_\beta = 1/5$ and initial perturbation $h'/H = 0.3$. The agreement between direct calculation and theoretical estimate based on the energy budget is good. On the other hand, in the two-layer moist model there is a gain of energy through latent heat release, with evaporation being an energy source in the system. The energy budget for the two-layer system is

$$\left.\begin{aligned} E_1 &= \int \mathrm{d}\boldsymbol{x}\left[\frac{|\boldsymbol{v}_1|^2}{2}h_1 + \frac{gh_1^2}{2}\right], \\ E_2 &= \int \mathrm{d}\boldsymbol{x}\left[\frac{|\boldsymbol{v}_2|^2}{2}h_2 + \frac{sgh_2^2}{2} + gh_1h_2\right], \\ \frac{\partial}{\partial t}(E_1+E_2) &= -\int \mathrm{d}\boldsymbol{x}\left[\mathcal{C}\left(gh_2(1-s) + \frac{|\boldsymbol{v}_1-\boldsymbol{v}_2|^2}{2}\right)\right], \end{aligned}\right\} \tag{4.6}$$

where $s = \theta_2/\theta_1$ is static stability, or stratification parameter, and E_i is the total energy of the i-th layer. Our numerical simulations indeed exhibit increasing energy, as follows from figure 13(*c*). We should, however, emphasize that the overall energy non-conservation remains small.

Thus, the energy diagnostics confirm the reliability of our numerical method.

5. Interactions of equatorial modons with their environment

5.1. *Kelvin-wave–modon interactions*

Kelvin waves travelling around the Equator on the sphere interact with the cyclonic dipoles, both being created by the moist equatorial adjustment process, as shown above. Let us first examine the dry adjustment in the one-layer model as a reference. The depression Kelvin wave produced by this process tends to form a sharp front at the rear (opposite to a fore-front in the elevation Kevin wave). The dissipation induced by such a Kelvin front generates potential vorticity (PV) anomaly, and thus a mean flow, as follows from the theoretical analyses (cf. McIntyre & Norton 1990; Le Sommer *et al.* 2004), and numerical simulations (Bouchut *et al.* 2005). In the simulation of the 'dry' adjustment presented in figure 14(*a*,*c*,*e*,*g*), we see the PV-anomaly dipoles and a weak westerly jet right behind the Kelvin front (at $\sim 60^\circ$ longitude), in accordance with Le Sommer *et al.* (2004) and Bouchut *et al.* (2005).

As the Kelvin wave propagates around the Equator, the interactions among the Kelvin wave, inertia-gravity waves and Rossby waves lead to a small-scale gravity-wave noise after one or two Kelvin wave circumrotations (it takes the dry Kelvin wave 12.5 days to travel around the Equator when $R_\beta = 1/5$).

When convection is turned on, ignoring evaporation, it is the moist potential vorticity moist potential vorticity (mPV), $(\zeta + f)/m$, with ζ being the vorticity, which is conserved (Lambaerts *et al.* 2011). One thus expects that dissipation in moist-convective Kelvin wave fronts also induce mean zonal flows. Figure 14(*b*,*d*,*f*,*h*) reveals two wave fronts associated with the moist Kelvin wave, the primary front around 150° longitude and a secondary one around 50° longitude at $t \approx 7$ days. The primary front is accompanied by a strong dipolar mPV anomaly which is stretching behind the front. Notice, however, that PV anomalies induced by the dry Kelvin front are mostly due to weak vorticity anomalies, while mPV anomalies induced by the moist Kelvin front are largely due to the moist enthalpy anomalies. The primary front is, at the same time, a moisture front,

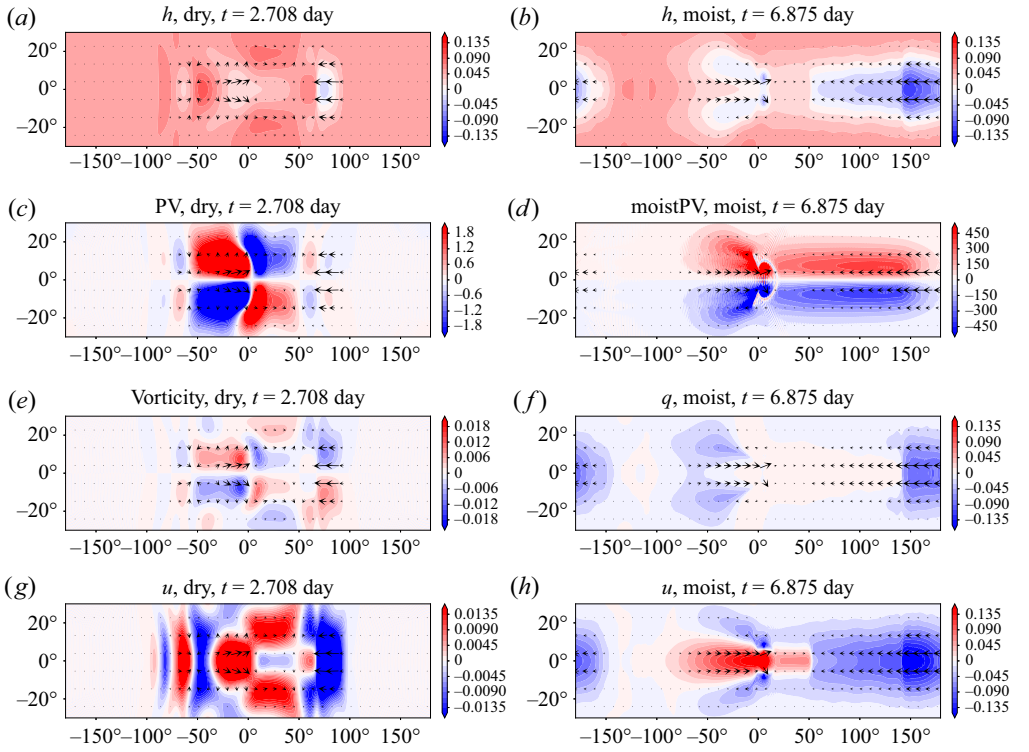

Figure 14. Snapshots of the dry (*a*,*c*,*e*,*g*) and moist-convective (*b*,*d*,*f*,*h*) adjustments in one-layer model, with Kelvin wave breaking. (*a*,*b*) Thickness anomaly h'/H, potential vorticity anomaly $[\zeta + f]h^{-1} - fH^{-1}$ (*c*), moist potential vorticity $[\zeta + f]m^{-1} - f[H - \tilde{Q}_0]^{-1}$ (*d*), relative vorticity (*e*) and moisture anomaly $[\tilde{Q} - \tilde{Q}_0]/\tilde{Q}_0$ (*f*), normalized zonal velocity $u/\sqrt{gH}$ (*g*,*h*). Here $R_\beta = 1/5$ and initial perturbation amplitude $h'/H = 0.1$. Notice the two orders of magnitude difference between (*c*) and (*d*) (the colour scheme for dry PV in (*c*) is chosen to better reveal the PV-anomaly dipole right behind the Kelvin front). Note that snapshots for the dry and the moist cases are chosen at different times to best visualize the Kelvin-wave-associated zonal wind anomalies.

as discussed in Bouchut *et al.* (2009), where a jump in moisture determines velocity jump. The difference with the dry Kelvin front is that the zonal flow is easterly, and not westerly, behind it, and there is an elongated negative thickness anomaly which is in approximate geostrophic equilibrium with this jet. On the contrary, the secondary front is more like a dry front, with a westerly flow behind, and no jump in moisture. It is, thus, the easterly jet right behind the primary Kelvin front which distinguishes moist and dry cases, and is a peculiar feature of the moist Kelvin wave breaking. As mentioned above, the baroclinic Kelvin moist front induces an easterly jet in the baroclinic mode, as well. The corresponding plots for the lower layer of the two-layer system look very similar to those for the one-layer system and are not shown.

In moist-convective environments, Rossby waves evolve into either eastward-moving equatorial modons or westward-moving twin cyclones, which interact with the Kelvin wave and associated easterly jets. We show the interaction between an eastward-moving modon and the Kelvin wave in figure 15. When the Kelvin wave approaches the cyclone pair, the resulting pattern is approximately a superposition of both, with a persistent positive zonal velocity at the centre of the cyclone pair (figure 15*g–i*). After one or two circumrotations of the Kelvin wave (it takes the moist-convective Kelvin wave

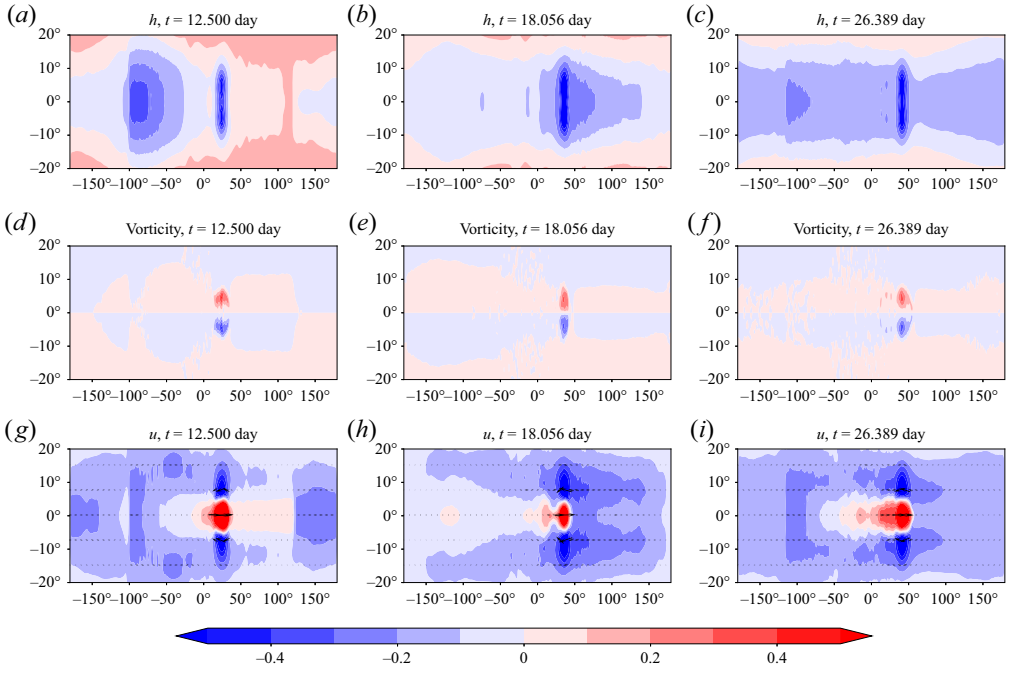

Figure 15. Interaction of the Kelvin waves with an equatorial modon in one-layer model. Panels (*a–i*) show h'/H, vorticity and normalized zonal velocity $u/\sqrt{gH}$. The vorticity field is reduced by 75 %, in order to have the same colourbar as for other fields. The apparent noisiness is due to strong compression in zonal direction applied in order to reveal Kelvin wave propagation, and is not of numerical origin (see figure 9 for a zoomed-in similar plot). Initial perturbation corresponds to figure 6(*g–h*).

15–17 days to travel around the Equator when $R_\beta = 1/5$), an easterly equatorial jet develops at all longitudes except near the modon. As a result, the modon turns into a westward-propagating twin-cyclone wave packet after propagating eastward for more than 30 days. We thus see that the interaction with the Kelvin wave strongly influences the eastward propagation of the modon.

The interference between the baroclinic Kelvin wave and the baroclinic modon reveals a similar effect in the two-layer model, as shown in figure 16 for the baroclinic mode of the two-layer model with $\delta = 0.2$, $R_\beta = 1/5$ and initial perturbation amplitude $h'/H_0 = 0.05$ ($h'/H_1 = 0.3$), which is a continuation of the simulation shown in figure 11(*c*,*d*). The adjustment process yields an equatorial modon that initially propagates eastward, yet reverses the direction of propagation after the first encounter with the moist Kelvin wave (figure 16*a*,*c*,*e*). However, if the zonal velocity associated with the baroclinic Kelvin wave is removed, i.e. the negative values of baroclinic zonal velocity are set to zero within the equatorial band 20°S–20°N, the modon continues its steady eastward propagation (figure 16*b*,*d*,*f*). This confirms that the zonal velocity due to the easterly mean flow induced by the moist Kelvin wave has a decisive influence upon the eastward translation of the modon. Notice that there is a secondary baroclinic modon generated to the east of the mature modon (figure 16*e*,*f*, more clearly visible when Kelvin-wave velocity is removed), similar to that observed in figure 9.

We display the interaction between westward-moving twin cyclones and moist Kelvin waves in figure 17, which shows the baroclinic mode of the two-layer model with $\delta = 1$, $R_\beta = 1/5$ and initial perturbation amplitude $h_1'/H_0 = 0.15$ ($h'/H_1 = 0.3$). As the

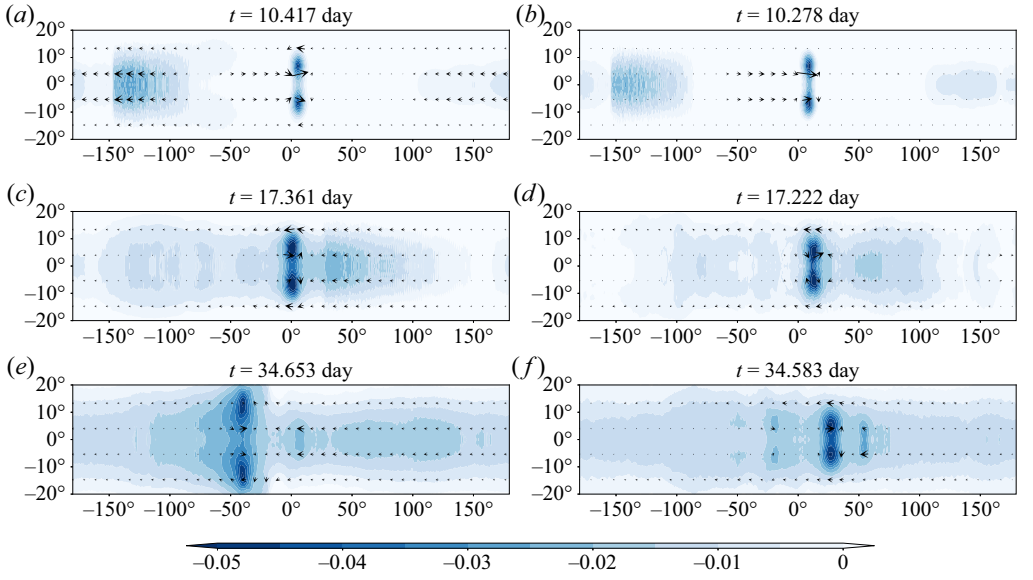

Figure 16. The effect of a baroclinic equatorial moist-convective Kelvin wave on long-time evolution of an equatorial modon. Shown is the baroclinic mode of thickness anomaly h'_-/H_0 in the two-layer model with $R_\beta = 1/5$, depth ratio $\delta = 0.2$ and initial perturbation amplitude ≈ 0.3. Panels (a,c,e) corresponds to the original simulation, and panels (b,d,f) to a simulation with the baroclinic Kelvin-wave velocity signal removed before the modon-Kelvin wave encounter, at $t \approx 10$.

Kelvin wave passes through the twin cyclones, zonal velocity at the centre of the cyclone pair turns from eastward to westward. After the passage of the Kelvin wave, the meridional distance between the twin cyclones abruptly increases, further weakening the nonlinear effect of mutual advection. The equatorial zonal velocity is more noisy, as compared with the previous case of a compact modon, although the zonal mean is still negative. Again, the moist Kelvin wave and its induced easterly jet strongly influence the propagation of twin cyclones, which can even disaggregate and produce a pair of separating intense vortices moving, respectively, north- and south-westward.

5.2. *Interaction of modons with a warm-pool and inductive generation of secondary cyclone pairs*

As was seen in figure 9, a secondary cyclone pair was generated eastward of the original equatorial modon, when $\tilde{Q}_s/H = 0.99$. This resembles, to some extent, the observed multiscale character of the MJO: the eastward-moving MJO pattern is composed of westward-moving mesoscale cloud clusters, with new clusters forming eastward of matured ones (Nakazawa 1988). It was, therefore, suggested that successive formation of new cloud clusters east of the matured-state cloud cluster might be responsible for the planetary-scale eastward motion. Although this hypotheses was disfavoured by Hendon & Liebmann (1994), it is worth examining closer the inductive generation of secondary cyclone pairs to the east of the matured 'parent' cyclone pairs. In particular, it is interesting to discriminate the origins of inductive generation: is it mostly due to enhanced local evaporation, like in the 'WISHE' mechanism (e.g. Emanuel 1987; Yano & Emanuel 1991; Emanuel 1993), or due to dynamical effects. Note that we do not have wind-induced

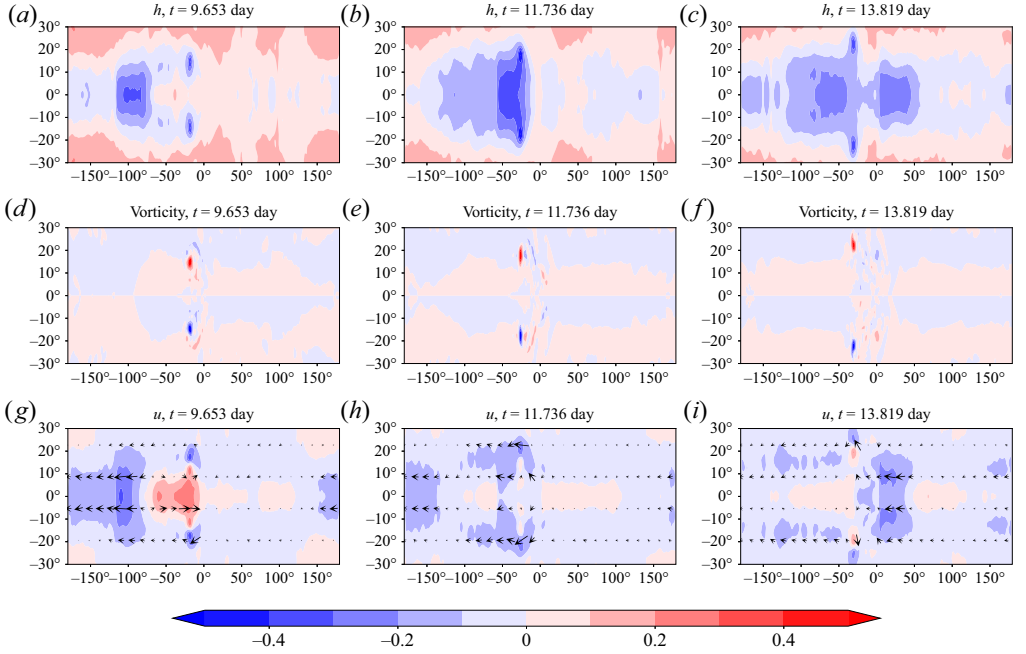

Figure 17. As in figure 15 but for the baroclinic mode of the two-layer system with depth ratio $\delta = 1$, $R_\beta = 1/5$ and initial perturbation amplitude $h_1'/H_0 = 0.15$. The value of thickness is multiplied by four in order to have the same colour code as other fields. Apparent noisiness is due to the zonal squeezing of the panels.

surface heat exchange (WISHE) mechanism except for its nonlinear version, as we do not prescribe a mean wind field.

We first present one-layer simulations displaying inductive generation of secondary cyclone pairs and then examine the sensitivity of this process with respect to variations of parameters. We found that the chance of generating secondary cyclone pairs greatly increases if we impose a spatial gradient of the background humidity $\tilde{Q}_0$. Introducing background humidity gradient could be rationalized by appealing to the gradients of the sea surface temperature due to the presence of a warm-pool. Recall that $\tilde{Q}_0$ was taken to be constant, and equal to 99 % $\tilde{Q}_s$ in the previous simulations. It now becomes

$$\tilde{Q}_0 = 0.99\,\tilde{Q}_s + \hat{Q}\left(\tilde{Q}_s \exp\left(-\left(\frac{r}{R_Q}\right)^2\right) - 1\right), \tag{5.1}$$

where $\hat{Q}$ is the amplitude of the variation of the background $\tilde{Q}_0$, R_Q is the warm-pool extent, and r is the distance to the centre of the warm-pool, which is placed at 0° longitude and 0° latitude. The maximum value of $\tilde{Q}_0$ is still 99 % $\tilde{Q}_s$.

A typical inductive generation of a secondary cyclone pair to the east of the parent dipole is shown in figure 18, where $\hat{Q} = 0.09$ and $R_Q = 4R_\beta \approx 45°$: the 'parent' cyclone pair moves to the west after an initial eastward propagation, so it returns to 0° longitude at $t = 18$ days, while the 'child' cyclone pair moves to the east while intensifying due to positive convective feedback. Note that at the early stages of inductive generation, local maxima in vorticity already appear just to the east of the mature cyclone pairs (figure 18*g*). Similar to what was seen above, condensation regions, in particular a chevron–like distribution around an equatorial modon, largely coincides with strong convergence areas

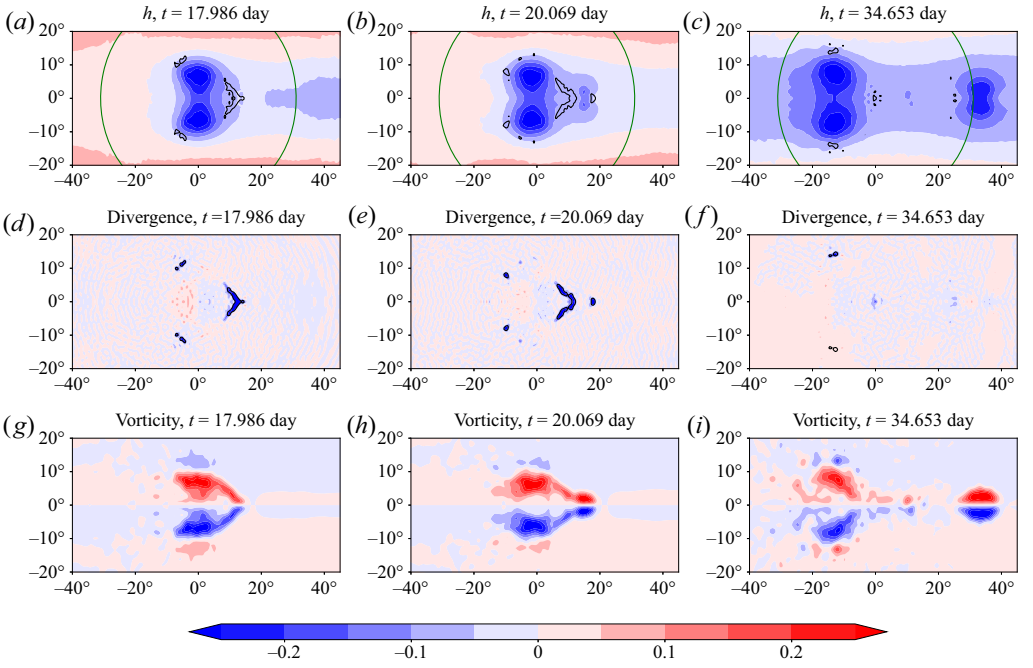

Figure 18. Inductive generation of secondary cyclone pairs to the east of matured cyclone pairs in the one-layer model. (*a–c*) thickness anomaly h'/H (colour), and condensation (contours). (*d–f*) divergence $\nabla \cdot \boldsymbol{v}$ (colour) and $\nabla \cdot (\boldsymbol{v}\tilde{Q})$ (contour lines). (*g–i*) vorticity (colours). The vorticity field is halved to share the colourbar with the pressure and divergence fields. The background water vapour field is described by (5.1), with $\hat{Q} = 0.09$ and $R_Q/a = 4R_\beta \approx 45^\circ$. The green contour in the top panel depicts the e-fold contour of $\tilde{Q}_0$. The increasing noise in the vorticity field, as time passes, suggests that the 'parent' cyclone pair decays by emitting Rossby and gravity waves, as it moves westward.

(note that the $\nabla \cdot (\boldsymbol{v}\tilde{Q})$ field pattern largely coincides with the $\nabla \cdot \boldsymbol{v}$ field pattern even with a spatial gradient of $\tilde{Q}_0$). This indicates that convergence provides most of the necessary moisture for condensation while evaporation is much smaller than condensation. We show condensation (figure 19*a*) and evaporation (figure 19*b*) at $t \sim 20$ days , which reveals an order of magnitude difference between the two. Given the relative weakness of evaporation, we can thus think in terms of the moist potential vorticity, which is conserved in the absence of evaporation.

The background mPV with $\tilde{Q}_0$ defined above, and the corresponding change in mPV due to the change in $\tilde{Q}_0$ are shown in figure 19(*c*,*d*). It is seen that the background humidity gradient sets up a background mPV gradient such that 0° longitude is the mPV maximum (minimum) at each latitude in the Northern (Southern) hemisphere. If a parcel is displaced toward the direction of decreasing background humidity or mPV in the Northern (Southern) hemisphere, it should gain positive (negative) vorticity to conserve mPV. Recalling that the zonal velocity at the centre of the parent cyclone pair is westerly, parcels there would be displaced eastward, experiencing a decrease in background mPV and hence gain positive (negative) vorticity in the Northern (Southern) hemisphere. Thus, the conservation of mPV readily explains the generation of a secondary vorticity maxima and cyclone pair to the east of the matured modon. Note that we observed an inductive generation in figure 9 (the case of $\tilde{Q}_s = 0.99H$) even without a spatially varying $\tilde{Q}_0$ or background mPV. In that case, the strong moist convection builds a warm-pool, right on

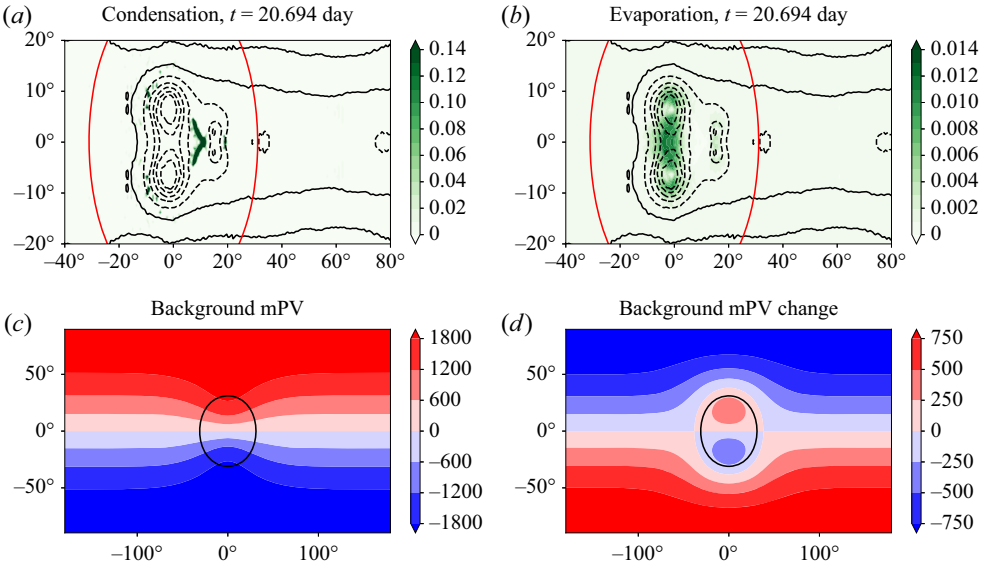

Figure 19. (*a*,*b*) Condensation (*a*) and evaporation (*b*) are shown in colours (note different colourbar range) while black contour lines depict the thickness anomaly h'/H field. (*c*,*d*) Background moist potential vorticity $mPV = f/[H - \cdot\tilde{Q}_0]$ (*c*), and the change in mPV due to changes in $\tilde{Q}_0$ (*d*). Red contours in the top panel delimit the warm-pool.

its eastern side in particular (cf. condensation right eastward of the matured modon in figure 18), and hence a moist potential vorticity gradient (not shown).

More simulations were conducted to test the robustness of the secondary generation. First, we slightly modify the warm-pool region by shrinking it in the meridional direction by half, while maintaining its zonal extent. Inductive generation to the east is also observed, but now the parent cyclone pair also moves to the east, at a greater phase speed due to its greater intensity, and collides/merges with the 'child' cyclone pair (figure 20*a–d*). Next, we enhance the spatial gradient of $\tilde{Q}_0$ by increasing $\hat{Q}$ to 0.15. The inductive generation is still robust yet the induced child cyclone pair is much weaker, and both the parent and child cyclone pairs move westward and poleward (figure 20*e–h*). Lastly, we test the robustness of inductive generation with respect to imposing the Clausius–Clapeyron relation by varying saturation vapour pressure with h', i.e. $\Delta\tilde{Q}_s/\tilde{Q}_{s0} = -0.1h'/H$, where $\tilde{Q}_{s0} = 0.9H$ is the constant saturation vapour pressure used in previous simulations. Still the secondary generation persists, and the parent cyclone pair and the child cyclone pairs tend to merge at later times.

The inductive generation also happens in the baroclinic mode of two-layer systems. As noted above, the baroclinic mode of the two-layer system with constant $\tilde{Q}_0$ also revealed such behaviour (a low-pressure lobe eastward of mature modons in figure 16*e*,*f*). We do not show results for the two-layer system with imposed spatial gradients in $\tilde{Q}_0$ or imposed background moist potential vorticity, but just note that they are consistent with those for one-layer models.

We should emphasize that simulations in the previous sections, which were shown to generate equatorial modons in a constant background moisture field, all exhibit the tendency to induce a secondary vorticity maxima, as in figure 18(*g*), which, however, often fails to develop into a clearly visible secondary equatorial modon. Thus, one can conclude

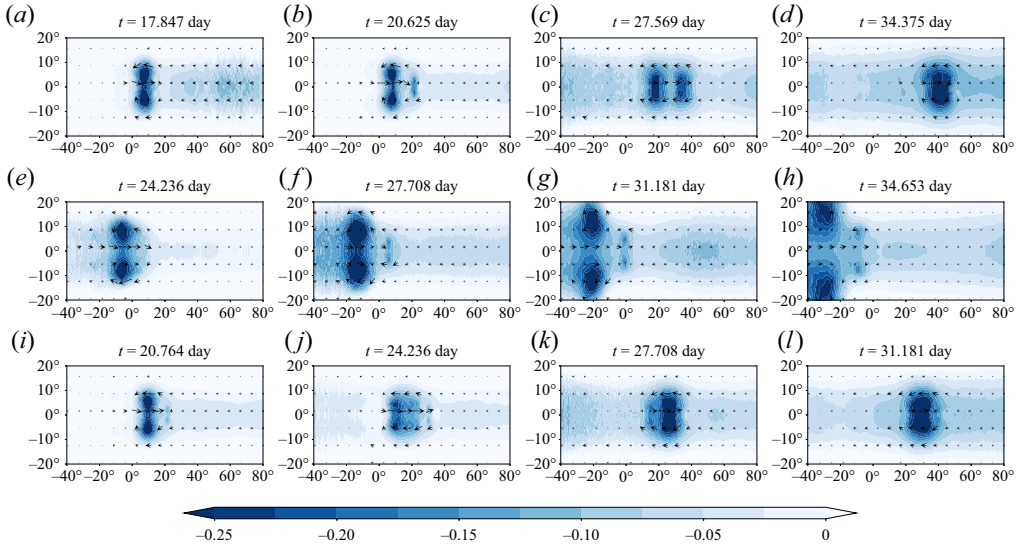

Figure 20. Inductive generation of secondary cyclone pairs to the east of matured cyclone pairs in three cases: warm-pool with zonal-to-meridional aspect ratio 2 (*a–d*), $\hat{Q} = 0.15$ (*e–h*) and varying saturation vapour pressure with h' (*i–l*). Colours: h'/H, with superimposed velocity vectors.

that inductive generation of a child cyclone pair to the east of a parent equatorial modon is a robust process, presumably due to the equatorial westerly flow associated with the cyclonic equatorial modon and the zonal gradient in moist potential vorticity resulting from the zonal gradient in the humidity field. On the other hand, in scenarios where cyclone pairs quickly split to move poleward (and westward) under the β-drift effect, we observe inductive generation neither in one-layer, nor in two-layer systems, even when $\tilde{Q}_0$ spatial gradient is imposed. This is because both the equatorial zonal velocity and $\tilde{Q}_0$ spatial gradient are relatively weak when the cyclone pair splits.

6. Discussion

Let us briefly summarize our main findings. First of all, we confirmed the existence of modon solutions in the dry one-layer RSW model on a sphere. We also showed that such solutions emerge as a result of the equatorial adjustment of localized depressions in the moist-convective one- and two-layer models in proper parameter regimes, thus demonstrating that earlier results are not an artifact of the beta-plane approximation. We also demonstrated the universality of the transient Gill pattern in the moist-convective environment in the one-layer model and in the baroclinic mode of the two-layer model before the eventual separation of the Kelvin and Rossby waves. The Rossby-wave response generates either eastward-moving modons, or westward-moving and meridionally separating twin cyclones. Our simulations reveal that the steepening of the circumnavigating moist Kelvin wave induces an extensive easterly jet, which strongly influences the dynamics in the Rossby-wave sector. Under the influence of the moist Kelvin waves, eastward-propagating modons tend to transform into westward-moving twin cyclones. These westward-moving twin cyclones differ from the previously known Boyd's solitons, which are composed of anticyclonic vortices and have faster phase speeds. We discovered an inductive generation of equatorial modons over oceanic warm-pools, and

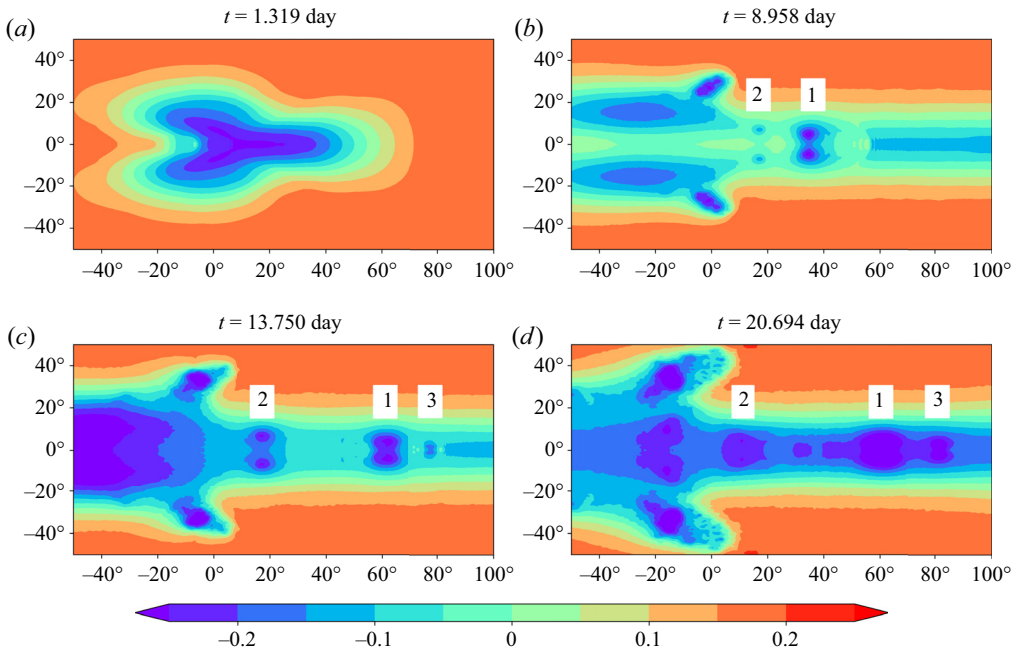

Figure 21. Adjustment process in one-layer mcRSW, with initial perturbation of amplitude ∼0.3 and size $2 \times aR_\beta$, as seen in the perturbation pressure h'/H. Background moisture field is constant, $\tilde{Q}_0 = 99\,\%\ \tilde{Q}_s$. Three cyclonic dipoles are labelled correspondingly. Here $R_\beta = 1/5$.

gave an explanation of this process on the basis of the conservation of moist potential vorticity.

The results of a complementary simulation of the equatorial adjustment in the one-layer shallow-water system with an initial perturbation of size $2 \times aR_\beta$, which is different from the previously used $1 \times aR_\beta$ perturbation, provides a good summary of our findings (figure 21). As before, we set $R_\beta = 1/5, h'/H \approx 0.3,\ \tilde{Q}_0 = 0.99\,\tilde{Q}_s$. At early stages ($t \approx 1.3$), we observe the planetary-scale transient Kelvin-Rossby hybrid structure, i.e. a transient version of the familiar Gill pattern. Subsequently, the Rossby-wave component becomes more compact and forms cyclone pairs due to the positive feedback between convection and circulation. Cyclone pairs '1' and '2' are generated at this stage, being compact enough to be called equatorial modons. While modon '1' moves eastward steadily, at a speed of ∼6 m s^{-1}, the weaker modon '2' reverses its direction later on and propagates westward. As modon '1' steadily moves eastward, it induces a child cyclone pair (labelled '3') to its east, due to the prevalent westerlies associated with the cyclone pairs.

One of the motivations of the present study was the hypothesis that MJO events could be represented by equatorial modons (Yano & Tribbia 2017). The mcRSW models are, obviously, too crude to grasp the MJO phenomenon in all its complexity. Although we concentrated above on the fundamental aspects of the dynamics of large-scale equatorial disturbances in the presence of moist convection, we believe that our results do have implications in the MJO context. Among them are the above mentioned universality and longevity of the transient planetary-scale Gill pattern, as a response to the initial pressure perturbations, the important role of circumnavigating Kelvin waves and the related mean flow (also see Haertel, Straub & Fedorov 2014; Haertel, Straub & Budsock

2015), and the hierarchical structure produced by inductive generation of cyclonic dipoles over warm-pools.

We should stress that the realism of mcRSW models can be augmented by including horizontal variations of temperature (Kurganov *et al.* 2020) and/or precipitable water (Rostami & Zeitlin 2018) in the models. The representation of thermodynamical phenomena and cloud-radiative feedbacks can be, correspondingly, ameliorated. The parameterizations of the boundary layer can be also improved (Schecter & Dunkerton 2009). These improvements could produce scenarios of equatorial adjustment closer to the observed MJO events, but we leave the exploration along these lines for further studies.

Acknowledgements. We thank G. Flierl for helpful discussion and suggestions.

Funding. The work of V.Z. was supported by the French National Program LEFE-IDAO. The work of B.Z. was supported by NASA Earth and Space Science Fellowship (NESSF) Program (18-EARTH18F-231). A.V.F. acknowledges grants from NASA (NNX17AH21G) and NOAA (NA20OAR4310377).

Declaration of interests. The authors report no conflict of interest.

Author ORCIDs.
Bowen Zhao https://orcid.org/0000-0003-4113-610X;
Vladimir Zeitlin https://orcid.org/0000-0001-7257-0844;
Alexey V. Fedorov https://orcid.org/0000-0001-5428-1117.

References

Arnold, N.P. & Randall, D.A. 2015 Global-scale convective aggregation: implications for the Madden–Julian oscillation. *J. Adv. Model. Earth Sy.* **7** (4), 1499–1518.

Baer, F. & Tribbia, J.J. 1977 On complete filtering of gravity modes through nonlinear initialization. *Mon. Weath. Rev.* **105** (12), 1536–1539.

Bouchut, F., Lambaerts, J., Lapeyre, G. & Zeitlin, V. 2009 Fronts and nonlinear waves in a simplified shallow-water model of the atmosphere with moisture and convection. *Phys. Fluids* **21** (11), 116604.

Bouchut, F., Le Sommer, J. & Zeitlin, V. 2005 Breaking of balanced and unbalanced equatorial waves. *Chaos* **15** (1), 013503.

Boyd, J.P. 1985 Equatorial solitary waves. Part 3: westward-traveling modons. *J. Phys. Oceanogr.* **15** (1), 46–54.

Charney, J.G. 1963 A note on large-scale motions in the tropics. *J. Atmos. Sci.* **20**, 607–609.

Emanuel, K. 1993 The effect of convective response time on WISHE modes. *J. Atmos. Sci.* **50** (12), 1763–1776.

Emanuel, K.A. 1987 An air-sea interaction model of intraseasonal oscillations in the tropics. *J. Atmos. Sci.* **44** (16), 2324–2340.

Fedorov, A.V. & Brown, J.N. 2009 Equatorial waves. In *Encyclopedia of Ocean Sciences*, pp. 271–287. Elsevier.

Fedorov, A.V. & Melville, W.K. 2000 Kelvin fronts on the equatorial thermocline. *J. Phys. Oceanogr.* **30** (7), 1692–1705.

Flierl, G.R., Larichev, V.D., McWilliams, J.C. & Reznik, G.M. 1980 The dynamics of baroclinic and barotropic solitary eddies. *Dyn. Atmos. Oceans* **5** (1), 1–41.

Flierl, G.R. 1978 Models of vertical structure and the calibration of two-layer models. *Dyn. Atmos. Oceans* **2** (4), 341–381.

Fuchs, Ž. & Raymond, D.J. 2002 Large-scale modes of a nonrotating atmosphere with water vapor and cloud–radiation feedbacks. *J. Atmos. Sci.* **59** (10), 1669–1679.

Fuchs, Z. & Raymond, D.J. 2005 Large-scale modes in a rotating atmosphere with radiative–convective instability and WISHE. *J. Atmos. Sci.* **62** (11), 4084–4094.

Fuchs, Ž. & Raymond, D.J. 2017 A simple model of intraseasonal oscillations. *J. Adv. Model. Earth Sy.* **9** (2), 1195–1211.

Gill, A. 1982 Studies of moisture effects in simple atmospheric models: the stable case. *Geophys. Astrophys. Fluid Dyn.* **19**, 119.

Gill, A.E. 1980 Some simple solutions for heat-induced tropical circulation. *Q. J. R. Meteorol. Soc.* **106** (449), 447–462.

HAERTEL, P., STRAUB, K. & BUDSOCK, A. 2015 Transforming circumnavigating Kelvin waves that initiate and dissipate the Madden–Julian oscillation. *Q. J. R. Meteorol. Soc.* **141** (690), 1586–1602.

HAERTEL, P., STRAUB, K. & FEDOROV, A. 2014 Lagrangian overturning and the Madden–Julian oscillation. *Q. J. R. Meteorol. Soc.* **140** (681), 1344–1361.

HECKLEY, W.A. & GILL, A. 1984 Some simple analytical solutions to the problem of forced equatorial long waves. *Q. J. R. Meteorol. Soc.* **110**, 203–217.

HENDON, H.H. & LIEBMANN, B. 1994 Organization of convection within the Madden–Julian oscillation. *J. Geophys. Res.: Atmos.* **99** (D4), 8073–8083.

HOSKINS, B.J. & BRETHERTON, F.P. 1972 Atmospheric frontogenesis models: mathematical formulation and solution. *J. Atmos. Sci.* **29** (1), 11–37.

JIANG, X., ADAMES, Á.F., KIM, D., MALONEY, E.D., LIN, H., KIM, H., ZHANG, C., DEMOTT, C.A. & KLINGAMAN, N.P. 2020 Fifty years of research on the Madden–Julian oscillation: recent progress, challenges, and perspectives. *J. Geophys. Res.: Atmos.* **125** (17), e2019JD030911.

KATSAROS, K. 2001 Evaporation and humidity. *Enc. Ocean Sci.* **1**, 870–877.

KHAIROUTDINOV, M.F. & EMANUEL, K. 2018 Intraseasonal variability in a cloud-permitting near-global equatorial aquaplanet model. *J. Atmos. Sci.* **75** (12), 4337–4355.

KIZNER, Z., REZNIK, G., FRIDMAN, B., KHVOLES, R. & MCWILLIAMS, J. 2008 Shallow-water modons on the f-plane. *J. Fluid Mech.* **603**, 305–329.

KURGANOV, A., LIU, Y. & ZEITLIN, V. 2020 Moist-convective thermal rotating shallow water model. *Phys. Fluids* **32**, 066601.

LAHAYE, N. & ZEITLIN, V. 2012 Existence and properties of ageostrophic modons and coherent tripoles in the two-layer rotating shallow water model on the f-plane. *J. Fluid Mech.* **706**, 71–107.

LAMBAERTS, J., LAPEYRE, G., ZEITLIN, V. & BOUCHUT, F. 2011 Simplified two-layer models of precipitating atmosphere and their properties. *Phys. Fluids* **23** (4), 046603.

LARICHEV, V.D. & REZNIK, G.M. 1976 On two-dimensional solitary Rossby waves. In *Doklady Akademii Nauk*, vol. 231, pp. 1077–1079. Russian Academy of Sciences.

LE SOMMER, J., REZNIK, G.M. & ZEITLIN, V. 2004 Nonlinear geostrophic adjustment of long-wave disturbances in the shallow-water model on the equatorial beta-plane. *J. Fluid Mech.* **515**, 135.

LECOANET, D., VASIL, G.M., BURNS, K.J., BROWN, B.P. & OISHI, J.S. 2019 Tensor calculus in spherical coordinates using Jacobi polynomials. Part-II: implementation and examples. *J. Comput. Phys: X* **3**, 100012.

LESOMMER, J., REZNIK, G.M. & ZEITLIN, V. 2004 Nonlinear geostrophic adjustment of long-wave disturbances in the shallow-water model on the equatorial beta-plane. *J. Fluid Mech.* **515**, 135–170.

LINDZEN, R.S. & NIGAM, S. 1987 On the role of sea-surface temperature gradients in forcing low-level winds and convergence in tropics. *J. Atmos. Sci.* **44** (17), 2418–2436.

MADDEN, R.A. & JULIAN, P.R. 1971 Detection of a 40–50 day oscillation in the zonal wind in the tropical Pacific. *J. Atmos. Sci.* **28** (5), 702–708.

MAJDA, A.J. & STECHMANN, S.N. 2009 The skeleton of tropical intraseasonal oscillations. *Proc. Natl Acad. Sci. USA* **106** (21), 8417–8422.

MANABE, S., SMAGORINSKY, J. & STRICKLER, R.F. 1965 Simulated climatology of a general circulation model with a hydrologic cycle. *Mon. Weath. Rev.* **93** (12), 769–798.

MATSUDA, Y. & TAKAYAMA, H. 1989 Evolution of disturbance and geostrophic adjustment on the sphere. *J. Meteorol. Soc. Jpn.* **67** (6), 949–966.

MATSUNO, T. 1966 Quasi-geostrophic motions in the equatorial area. *J. Meteorol. Soc. Jpn.* **44** (1), 25–43.

MCINTYRE, M.E. & NORTON, W.A. 1990 Dissipative wave-mean interactions and the transport of vorticity or potential vorticity. *J. Fluid Mech.* **212**, 403–435.

MULLER, C.J., BACK, L.E., O'GORMAN, P.A. & EMANUEL, K.A. 2009 A model for the relationship between tropical precipitation and column water vapor. *Geophys. Res. Lett.* **36** (16), L16804.

NAKAZAWA, T. 1988 Tropical super clusters within intraseasonal variations over the western Pacific. *J. Meteorol. Soc. Jpn.* **66** (6), 823–839.

NEELIN, J.D. & YU, J.-Y. 1994 Modes of tropical variability under convective adjustment and the Madden–Julian oscillation. Part I: analytical theory. *J. Atmos. Sci.* **51** (13), 1876–1894.

RANDALL, D. 2015 *An Introduction to the Global Circulation of the Atmosphere*. Princeton University Press.

RAYMOND, D.J. & FUCHS, Ž. 2009 Moisture modes and the Madden–Julian oscillation. *J. Clim.* **22** (11), 3031–3046.

REZNIK, G.M. & GRIMSHAW, R. 2001 Ageostrophic dynamics of an intense localized vortex on a beta-plane. *J. Fluid Mech.* **443**, 351–376.

RIBSTEIN, B., GULA, J. & ZEITLIN, V. 2010 (A)geostrophic adjustment of dipolar perturbations, formation of coherent structures and their properties, as follows from high-resolution numerical simulations with rotating shallow water model. *Phys. Fluids* **22**, 116603.

ROSTAMI, M. & ZEITLIN, V. 2018 An improved moist-convective rotating shallow-water model and its application to instabilities of hurricane-like vortices. *Q. J. R. Meteorol. Soc.* **144** (714), 1450–1462.

ROSTAMI, M. & ZEITLIN, V. 2019*a* Eastward-moving convection-enhanced modons in shallow water in the equatorial tangent plane. *Phys. Fluids* **31** (2), 021701.

ROSTAMI, M. & ZEITLIN, V. 2019*b* Geostrophic adjustment on the equatorial beta-plane revisited. *Phys. Fluids* **31** (8), 081702.

ROSTAMI, M. & ZEITLIN, V. 2020*a* Can geostrophic adjustment of baroclinic disturbances in tropical atmosphere explain MJO events? *Q. J. R. Meteorolog. Soc.* **146** (733), 3998–4013.

ROSTAMI, M. & ZEITLIN, V. 2020*b* Eastward-moving equatorial modons in moist-convective shallow-water models. *Geophys. Astrophys. Fluid Dyn.* 1–23.

SCHECTER, D.A. & DUNKERTON, T.J. 2009 Hurricane formation in diabatic Ekman turbulence. *Q. J. R. Meteorol. Soc.* **135** (641), 823–838.

SEAGER, R. 1991 A simple model of the climatology and the variability of the low-level wind field in the tropics. *J. Clim.* **4**, 164–179.

SUTYRIN, G.G. & FLIERL, G.R. 1994 Intense vortex motionon the beta plane: development of the beta gyres. *J. Atmos. Sci.* **51**, 773–790.

TRIBBIA, J.J. 1984 Modons in spherical geometry. *Geophys. Astrophys. Fluid Dyn.* **30** (1–2), 131–168.

VASIL, G.M., LECOANET, D., BURNS, K.J., OISHI, J.S. & BROWN, B.P. 2019 Tensor calculus in spherical coordinates using Jacobi polynomials. Part-I: mathematical analysis and derivations. *J. Comput. Phys: X* **3**, 100013.

VERKLEY, W.T.M. 1984 The construction of barotropic modons on a sphere. *J. Atmos. Sci.* **41** (16), 2492–2504.

WEDI, N.P. & SMOLARKIEWICZ, P.K. 2010 A nonlinear perspective on the dynamics of the MJO: idealized large-eddy simulations. *J. Atmos. Sci.* **67**, 1202–1217.

WHEELER, M. & KILADIS, G.N. 1999 Convectively coupled equatorial waves: analysis of clouds and temperature in the wavenumber-frequency domain. *J. Atmos. Sci.* **56** (3), 374–399.

YANG, D. & INGERSOLL, A.P. 2011 Testing the hypothesis that the MJO is a mixed Rossby–gravity wave packet. *J. Atmos. Sci.* **68** (2), 226–239.

YANG, D. & INGERSOLL, A.P. 2013 Triggered convection, gravity waves, and the MJO: a shallow-water model. *J. Atmos. Sci.* **70** (8), 2476–2486.

YANG, D. & INGERSOLL, A.P. 2014 A theory of the MJO horizontal scale. *Geophys. Res. Lett.* **41** (3), 1059–1064.

YANO, J.-I. & BONAZZOLA, M. 2009 Scale analysis for large-scale tropical atmospheric dynamics. *J. Atmos. Sci.* **66** (1), 159–172.

YANO, J.-I. & EMANUEL, K. 1991 An improved model of tropical troposphere and its coupling with the stratosphere. *J. Atmos. Sci.* **48** (3), 377–389.

YANO, J.-I., MULET, S. & BONAZZOLA, M. 2009 Tropical large-scale circulations: asymptotically non-divergent? *Tellus A* **61**, 417–427.

YANO, J.-I. & TRIBBIA, J.J. 2017 Tropical atmospheric Madden–Julian oscillation: a strongly nonlinear free solitary Rossby wave? *J. Atmos. Sci.* **74** (10), 3473–3489.

ZEITLIN, V. 2018 *Geophysical Fluid Dynamics: Understanding (almost) Everything with Rotating Shallow Water Models*. Oxford University Press.

ZHANG, C. 2005 Madden–Julian oscillation. *Rev. Geophys.* **43** (2), RG2003.

ZHANG, C., ADAMES, Á.F., KHOUIDER, B., WANG, B. & YANG, D. 2020 Four theories of the Madden–Julian oscillation. *Rev. Geophys.* **58** (3), e2019RG000685.